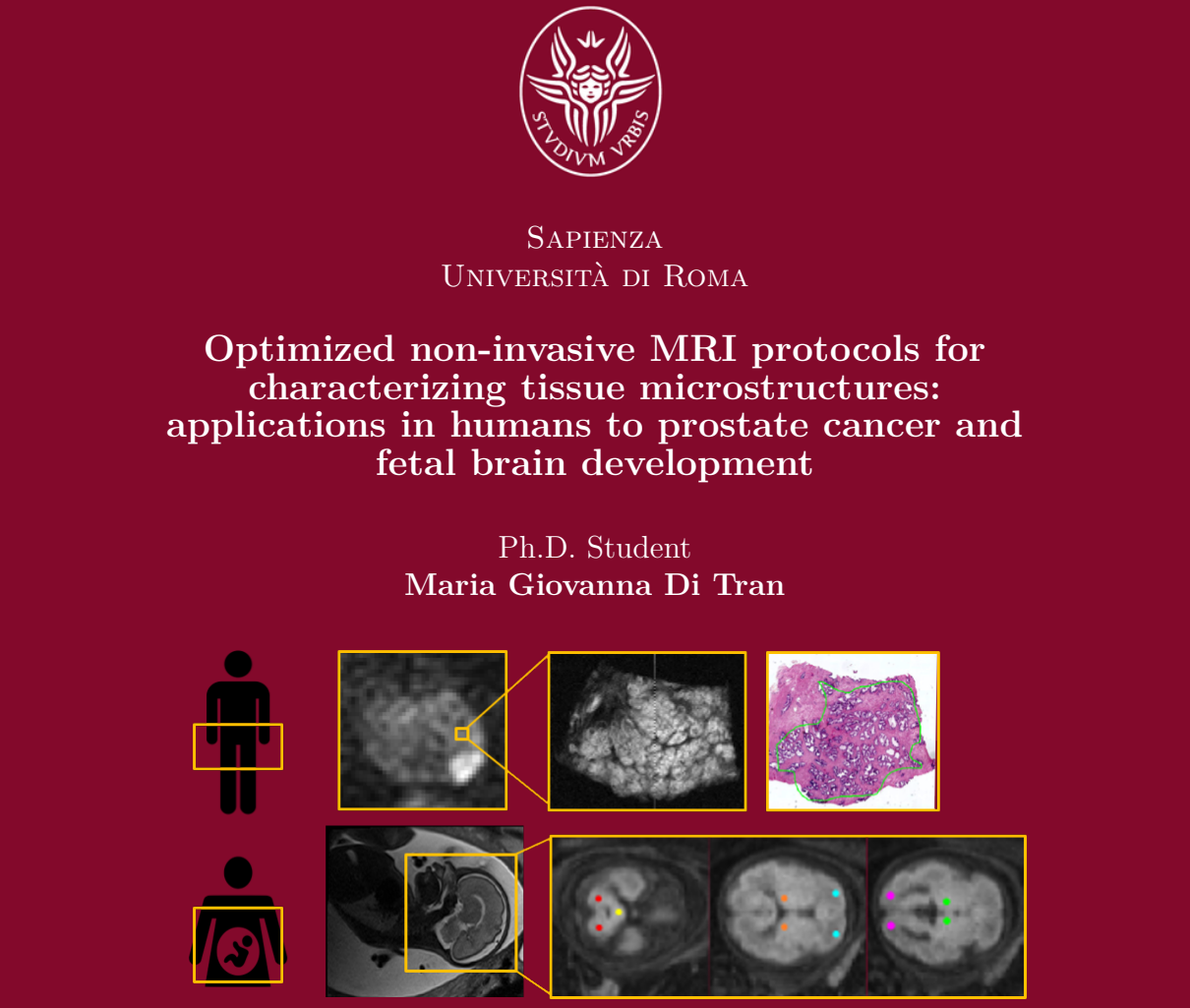

Sapienza
Università di Roma

Optimized non-invasive MRI protocols for characterizing tissue microstructures: applications in humans to prostate cancer and fetal brain development

Ph.D. Student
Maria Giovanna Di Tran

Advisor:
Prof. Silvia Capuani
Co-advisor:
Prof. Silvia Mangia

Coordinator:
Prof. Antonio Musarò

SAPIENZA
UNIVERSITÀ DI ROMA

UNIVERSITÀ DEGLI STUDI DI ROMA
LA SAPIENZA

PH.D. IN MORPHOGENESIS AND TISSUE ENGINEERING
XXXII CYCLE - CURRICULUM IN BIOPHYSICS

Optimized non-invasive MRI protocols for characterizing tissue microstructures: applications in humans to prostate cancer and fetal brain development

Ph.D. Student
Maria Giovanna Di Trani

Advisor:
Prof. Silvia Capuani
Co-advisor:
Prof. Silvia Mangia

Coordinator:
Prof. Antonio Musarò

February 2020

A mia madre

Contents

Introduction

In the last two decades, Magnetic resonance imaging (MRI) revolutionized medical diagnostic, providing exquisite three dimensional images of the human body and demonstrating to be sensitive to a wide spectrum of diseases.
The innovation and power of this technique lies in its ability to provide quantitative information on living systems without damaging their structures or perturbing their physiological processes, rather enabling the investigation of biological systems at their equilibrium.
MRI benefits from being a flexible technique, since by changing parameters used for the image acquisition, it is possible to investigate different tissue properties and obtain different image contrasts. This unique characteristic stems from the fact that the MRI signal depends on several properties of the tissue, distinguishing MRI from other types of radiological imaging, such as computed tomography (CT) where the image is a map of only one tissue property, the X-ray absorption coefficient.
The very first applications of MRI were dedicated to the study of the brain; however, at the end of the 1990s, the introduction of echo planar imaging (EPI) provided sequences able to perform acquisitions during a single breath hold, paving the way to MRI applications in abdominal regions, where hearth-beat and breathing cause image artifacts.
Thanks to the introduction of EPI and to the versatility of MRI, sequences developed for brain imaging were adapted to image different body organs or structures, such as heart, lungs, liver, stomach, breast, prostate, knee, muscles, bones, placenta, blad-

der and even teeth.
The work presented in this thesis was dedicated to the optimization of several MRI protocols for the examination of the human pelvis, involving the definition of procedures with high diagnostic potential.
In particular, in this work we exploited the versatility of MRI to investigate the evolution of prostate cancer (PCa), the second most common malignancy among men worldwide.
The study of prostate cancer was conducted by employing several MRI techniques with the aim to characterize the microstructures and microenvironment of the tissue. The main part of the study was dedicated to develop new MRI techniques for clinical applications, in order to improve the sensitivity of the diagnostic.
In order to explore the structural organization of prostate tissue, we performed Diffusion Magnetic Resonance Imaging (DMRI), a technique that exploits the physiologic motion of water molecules in biologic system to provide exquisite information on tissue architecture. In particular, our study focused on the diagnostic application of Diffusion Tensor Imaging (DTI), compared to a relatively recent technique, Diffusion Kurtosis Imaging (DKI).
Given the sensitivity of this DMRI for microstructures, we investigated the possibility to classify PCa aggressiveness by estimating the water mean diffusivity (MD) of the lesion employing different diffusion weightings, i.e. b-values, during the image acquisition. Our results showed that increasing the diffusion weighting, we improved the sensitivity of the diffusion parameters for the classification of tumor aggressiveness. This result motivated our interest in performing DKI, a technique that capture water diffusion features when high diffusion weightings are employed, providing additional information on tissue microstructure, inaccessible to DTI technique. A particular attention was dedicated to the image quality during the acquisition and postprocessing, to address the well-known drawback of the low signal-to-noise ratio of high b-values acquisitions.
Experiments with DMRI were conducted both in-vivo, on human subjects affected by PCa of different grades, and ex-vivo on hu-

man tissue samples obtained after prostatectomy surgery.
By using the water molecular diffusion as endogenous contrast mechanism, with DMRI technique it is possible to probe tissue architecture at microscopic scale. However, in clinical imaging, all micro-scale information are averaged out in pixels with the dimension of 1-2mm. In this study, experiments of high-resolution (70x70μm in plane) DMRI were conducted ex-vivo on human tissue samples obtained after prostatectomy surgery, by using a high-field MRI scanner. This experiment represented the unique opportunity to image the glandular structure of prostate and estimate DTI and DKI parameters in the different micro-compartments of the gland, thanks to a direct comparison with the histology images.
The second part of this PhD project was dedicated to develop new MRI sequences for prostate imaging at the Center for Magnetic Resonance Research (CMRR) in Minneapolis. The study conduced at the CMRR aimed at providing new contrast mechanism for prostate cancer imaging, based on $T_1\rho$ and $T_2\rho$ relaxation times. Compared to the conventional T_1 and T_2 time constant, amply used in clinics, $T_1\rho$ and $T_2\rho$ characterize the relaxation of the nuclear magnetization in the rotating frame and they are sensitive to molecular dynamics occurring at lower frequencies, typically kHz. This range of frequencies is characteristic of several in-vivo processes, such as the interaction between free water and macromolecules, enabling the access to important information on tissue microenvironment.
However, performing $T_1\rho$ and $T_2\rho$ imaging is limited by the intensive energy deposited by the acquisition sequence, which is usually overcome by increasing the acquisition time, preventing the possibility of diagnostic applications. The novelty of our approach was to perform imaging in the rotating frame with a three-dimensional acquisition method recently developed at the CMRR, in order to address the aforementioned shortcoming of long acquisition time.
Leveraging on a multi-modal approach, this project will explore the potentiality of new contrast mechanisms, beyond the conven-

tional clinical imaging, to a non-invasive staging of PCa.
In a parallel and exciting project, DMRI was performed to investigate the mechanism of brain development during the fetal growth. Thanks to the safety of MRI, the apparent diffusion coefficient was measured in fetuses during the second and third week of gestation. The study was focused not only on the healthy fetal brain development, but also explored cases of abnormal brain maturation in fetuses with ventriculomegaly, a common disease, diagnosed at any gestational age, consisting in an irregular enlargement of ventricles, diagnosed at any gestational age. Brain tissue, as well as prostate gland, like other biological tissues, consists of a heterogeneous structural organization, due to cell boundaries and macromolecular crowding. Therefore, employing a non-Gaussian imaging technique, such as DKI, would have been optimal to characterize the complexity of brain structures. However, the necessity to design a short fetal image protocol to minimize artifacts due to motion, prevented to perform non-Gaussian imaging and motivated the choice to combine a fast acquisition protocol with a post-processing pipeline, dedicated to improve image quality. This study was encouraged by the well known sensitivity of DMRI for tissue microstructural changing and it will be discussed in the last chapter as a separate section.

Chapter 1

Introduction to MRI

Magnetic resonance imaging (MRI) is one of the most powerful and versatile imaging techniques, whose impact in science lies in its ability of giving information about process at the atomic level, providing a fundamental tool for many fields, such as chemistry, physics, medicine and psychology.
Magnetic resonance is a physical phenomenon occurring when nuclei in an external magnetic field exchange electromagnetic energy. This phenomenon was independently discovered by Purcell and Bloch in 1946, earning them the Nobel Prize.
At the beginnings, MR was exploited to determine the magnetic moments of nuclei and contribute to the study of solid and liquid materials. Later, thanks to the introduction of pulsed NMR in combination with Fourier transformation, MR becomes one of the most important techniques for medical imaging, drastically improving the sensitivity of clinical diagnostic.

1.1 Imaging principles

Magnetic resonance is a physical phenomenon exhibited by magnetic systems that possess magnetic moment, called *spin*, and angular momentum. It occurs when nuclei in an external magnetic field absorb and emit electromagnetic radiation.

When protons or neutrons combine to form a nucleus, they pair with oppositely oriented spins; therefore, only nuclei with an odd number of nucleons do have a net magnetic moment. One of these is hydrogen, that became consequently the primary focus of MRI studies in biologic systems given its abundance in the body.
When a nucleus with magnetic moment is placed in a magnetic field, it precesses around the field axes with its own resonant frequency, called the Larmor frequency (Fig. 1.1 A)

$$\omega_0 = \gamma B_0, \tag{1.1}$$

directly proportional to the strength of the external magnetic field B_0 and the gyromagnetic ratio γ, a constant factor specific for each nucleus. For nuclear spins, the magnetic resonance frequency falls typically in the radio-frequency region (5-900MHz).
Any MRI experiment consists of four principal steps: the preparation of the sample in the external magnetic field, the excitation caused by a radio frequency (RF) pulse, the spatial encoding and signal acquisition. Let's imagine a very simple experiment with a sample placed in a large magnetic field and a coil, that works as both a transmitter and a receiver, placed close to the sample with its axis perpendicular to the magnetic field. During the transmit or excitation phase, a RF pulse oscillating at the same resonance frequency of the nuclei is applied to the sample for few milliseconds. In the resonance condition, nuclei are able to absorb electromagnetic energy from the RF pulse and return a portion of that energy to the coil as an induced oscillating current.
In order to understand what happened to the sample, we should consider the dynamic of the sample spins as a collection of magnetic dipoles in a magnetic field. The ensemble of spins may be conveniently described in terms of the spin magnetization vector **M**, that is the sum over all spin magnetic moments [1].
The effect the magnetic field **B** exerts on the dipoles it's a torque that tends to align spins along the field axis, described mathematically by the rate of change with time of the angular momentum

vector $\mathbf{M}/\gamma$:

$$\frac{d\mathbf{M}}{dt} = \gamma \mathbf{M} \times \mathbf{B}. \tag{1.2}$$

The dynamic described by the solution of the preceding equation corresponds to a precession of the magnetization about the field at rate $\omega_0 = \gamma B_0$ (typically in the order of MHz), where B_0 is the static magnetic field amplitude. The source of this precession is due to the fact that nuclear dipoles possess angular momentum in addition to a magnetic moment.

At the equilibrium, the magnetic dipoles are aligned in the same

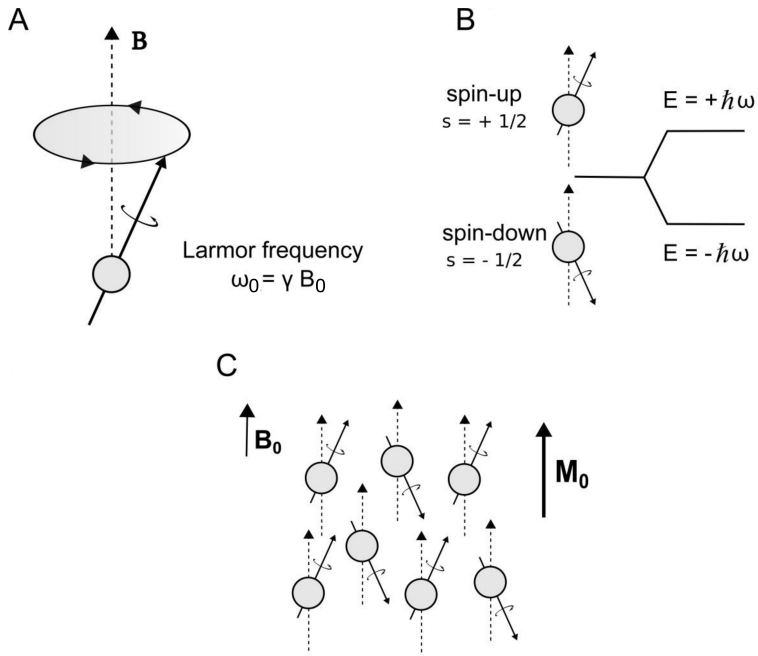

Figure 1.1: *Spins in an external magnetic field* ***B*** *precess at the Larmor frequency (A) with their axis oriented in the same or in the opposite direction to the field, in two energetic states (B) whose difference in energy generates a net magnetization* M_0 *(C).)*

or in the opposite direction of the field, in two different energetic states (Fig. 1.1 B). The rate of the population distribution of the

two spin states is given by the Boltzmann distribution

$$\frac{N_+}{N_-} = e^{-\Delta E/K_B T}, \tag{1.3}$$

where N_+ is the number of spins in the $m = \frac{1}{2}$ state and N_- in the $m = -\frac{1}{2}$ state.
The induced energy difference between the spins aligned and those opposed to the field at 1.5 T is only approximately 1% of the random thermal energy of the sample molecules, as a result the energy absorption is very low, making NMR a non-invasive and non-destructive technique, ideal for in-vivo measurements.
This energy difference creates a weak longitudinal magnetization M_0 aligned with the field (Fig. 1.1 C), directly proportional to the local proton density. At thermal equilibrium, in presence of the only static magnetic field, from the equation (1.2), we deduce that the the longitudinal magnetization is constant, $\frac{dM_z}{dt} = 0$, while there is no net magnetization in the transverse plane $M_{x,y} = 0$, since spins have no phase coherence. The longitudinal magnetization is not directly measurable, because it is many orders of magnitude weaker than the static magnetic field B_0.
To measure the nuclear magnetization the system is excited by an oscillating magnetic field B_1 perpendicular to B_0. In general, the field B_1 is several orders of magnitude smaller than B_0 and it's generated in the coil by an RF current oscillating at the resonance frequency ω_0. The effect of B_1 is to tip the magnetization away from B_0, generating a nonzero transverse magnetization $M_{x,y} = 0$. After the excitation, $\mathbf{M}$ begins to precess around the net field generated by the sum of B_1 and B_0, drawing a growing spiral (Fig. 1.2), until the the system relaxes to a new equilibrium state where the magnetization is recovered to its initial value M_0.
This relaxation process, know as *spin-lattice relaxation*, involves an exchange of energy between the spin system and the surrounding environment. The magnetization components M_x, M_y, M_z return to thermal equilibrium in an exponential manner, but with two different time constants T_1 and T_2, characteristic for each

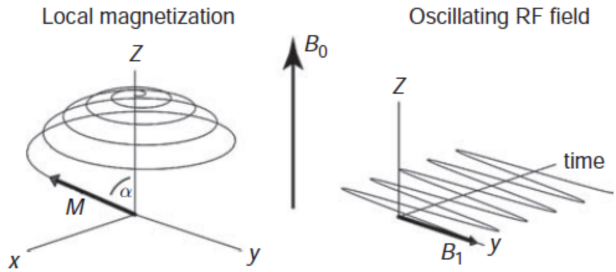

Figure 1.2: *The RF pulse B_1 oscillating perpendicular to B_0 causes the magnetization $\boldsymbol{M}$ to precess around the net field, tracing a spiral. The flip angle α is determined by the strength and duration of B_1. [18].*

tissue:

$$\frac{dM_x}{dt} = \gamma B_0 M_y - \frac{M_x}{T_2} \tag{1.4a}$$

$$\frac{dM_y}{dt} = -\gamma B_0 M_x - \frac{M_y}{T_2} \tag{1.4b}$$

$$\frac{dM_z}{dt} = -\frac{M_z - M_0}{T_1} \tag{1.4c}$$

The longitudinal relaxation process concerns the exchange of energy from nuclear spins to the environment and it's characterized by the time constant T_1. Whereas, the relaxation of the transverse magnetization is caused by the loss of phase coherence between spins exchanging energy between themselves and it's ruled by the time constant T_2.
The equations 1.4 were formulated by Bloch as phenomenological equations that describe the behaviour of the nuclear magnetization in the magnetic field, already described by Eq. 1.2, taking into account the relaxation process.
During the process of relaxation generated by the RF pulse, the precessing magnetization produces a magnetic field, variable in time, that induces in a nearby receiver coil a small electromotive force, via Faraday's law. This detectable signal is called a *free induction decay* and represent the basic MR signal [13, 19].

It's evident at this point that the MR signal depends on several intrinsic properties of the tissue, such as proton density and relaxation times, making MRI technique sensitive to different tissue parameters and image contrasts.

1.1.1 Signal localization

Summarizing, a basic MR experiment consists of applying a brief RF pulse to the sample and monitoring the current induced in the coil, however in order to create an image, it's necessary to reconstruct the spatial distribution of the FID signal.
The localization of the signal is based on the direct proportionality relationship between the resonant frequency and the magnetic field. By applying magnetic field gradients, in addition to the static magnetic field and the RF pulse, it is possible to control the local magnetic field, then the local resonant frequency.
Therefore, in a MR scanner there are three additional coils, *gradient coils*, each of which produces a magnetic field that varies linearly along a particular axis.
In presence of the magnetic field gradients $\mathbf{G}$, we can define a *local* Larmor frequency

$$\omega(\boldsymbol{r}) = \gamma B_0 + \gamma \boldsymbol{G} \cdot \boldsymbol{r} \tag{1.5}$$

where $\boldsymbol{G} = \left(\frac{\partial B_z}{\partial x}, \frac{\partial B_z}{\partial y}, \frac{\partial B_z}{\partial z}\right)$.
This simple relation covers a fundamental role in the MR imaging: it allows to link the signal with the spins position within the sample.
The received time signal $S(t)$ is derived from the contributions of all precessing spins in the volume. Considering that, the signal equation *on resonance*[1] may be written as

$$S(t) = \iiint \rho(\boldsymbol{r}) e^{i\gamma \boldsymbol{G}\cdot\boldsymbol{r}t} d\boldsymbol{r} \tag{1.6}$$

[1] On resonance, condition is obtained choosing γB_0 as the reference frequency. In the *off resonance* condition the signal would be $S(t) = \iiint \rho(\boldsymbol{r}) e^{i(\gamma B_0 + \gamma \boldsymbol{G}\cdot\boldsymbol{r})t} d\boldsymbol{r}$

where $\rho(\boldsymbol{r})$ is the local spin density at the position $\boldsymbol{r}$.
Introducing the concept of the reciprocal space vector $\boldsymbol{k}$

$$\boldsymbol{k} = \frac{\gamma \boldsymbol{G} t}{2\pi} \tag{1.7}$$

and using the Fourier transform, we obtain a fundamental relationship for the NMR imaging:

$$S(\boldsymbol{k}) = \iiint \rho(\boldsymbol{r}) e^{i2\pi \boldsymbol{k}\cdot\boldsymbol{r}} d\boldsymbol{r} \tag{1.8}$$

$$\rho(\boldsymbol{r}) = \iiint S(\boldsymbol{k}) e^{-i2\pi \boldsymbol{k}\cdot\boldsymbol{r}} d\boldsymbol{k}. \tag{1.9}$$

These relations state that the proton density image can be obtained with the inverse Fourier transform of the detected NMR signal.
The image reconstruction is accomplished by sampling the signal in the **k**-space.
In a three dimensional space, the sampling leads to a collection of N^3 data points that assembles a 3-D matrix, whose dimensions k_x,k_y and k_z ranges in $[-\frac{1}{2}N\Delta k, (\frac{1}{2}N-1)\Delta k$, with the sampling interval $\Delta k = 2k_{max}/N$.
In the real space, the image $\rho(\mathbf{r})$ is represented by a 3-D conjugate matrix whose dimensions x,y and z ranges in $[-\frac{1}{2}N\Delta l, (\frac{1}{2}N-1)\Delta l]$, with $\Delta l = 2l_{max}/N$ as the sampling interval.
The two conjugate matrices (Figure 1.3) are connected by the Fourier transformation, then the resolution in real space is determined by the sampling range

$$\Delta l = \frac{1}{2k_{max}}. \tag{1.10}$$

Moreover, the field of view (FOV) in real space is given by

$$FOV = \frac{1}{\Delta k} = \frac{N}{2k_{max}}. \tag{1.11}$$

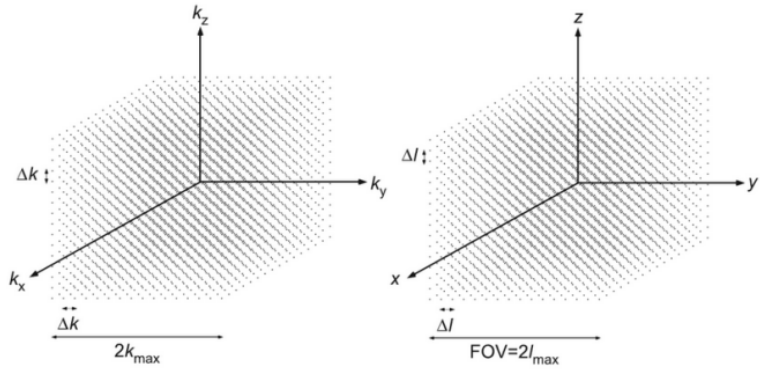

Figure 1.3: *Conjugate matrices of the* ***k****-space on the left and the real space on the right [20].*

It's important to note that time and gradient magnitude can be varied to traverse the **k**-space. This is fundamental for the signal localization that is realized in three steps, corresponding to the spatial dimensions: *slice selection*, *frequency encoding* and *phase encoding*.

Slice Selection The slice selection permits to excite a single slice of the entire volume. This is achieved by applying, simultaneously to the RF pulse, a gradient field G_z with an amplitude that linearly varies with the z-position. As a consequence, the Larmor frequencies of the spins will have a spatial dependence

$$\omega(z) = \gamma B_0 + \gamma G_z z \tag{1.12}$$

Then, only those spins residing in z-locations with resonant frequency matching the bandwidth of B_1 will be excited.
The RF pulse is shaped like truncated sinc function $\sin x/x$, in this way its Fourier transform, a rectangle, approximates the slice profile.
The slice location can be varied by changing the center frequency ν_0 of the RF pulse (Fig. 1.4). The slice thickness depends on the ratio of the RF pulse bandwidth to the field gradient strength. Typically, the slice width is modified by changing the gradient strength, so its thickness range is generally $1 - 10mm$.

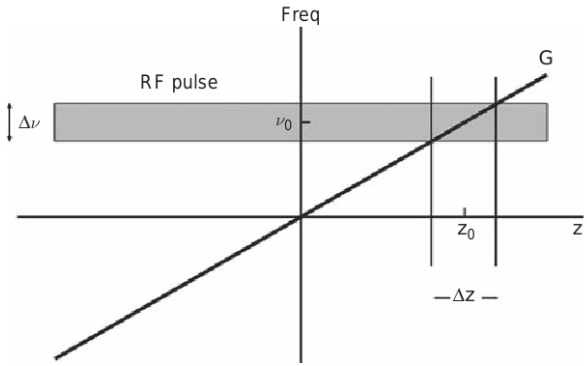

Figure 1.4: *When a RF pulse with a narrow bandwidth $\Delta\nu$ is applied in the presence of a z-gradient, only spins within a band of positions Δz are excited [18].*

Frequency and phase encoding After the slice selection, the signal must be localized in the $x - y$ plane with frequency and phase encoding, based on Eq. 1.12.
Using the gradients G_x and G_y, it is possible to sample k-space with several trajectories.
In Figure 1.5 it is represented an example of one of the possible trajectory for a spin echo sequence in the conjugate space:

1. after the excitation, two gradient pulses in the x and y directions provoke a phase traverse to a point of the (k_x, k_y) determined by the gradients amplitude;

2. a 180° RF pulse inverts all the spins phases creating an echo;

3. G_x is turned on during data collection, for this reason is also called the *read-out gradient*.

G_x is responsible for the frequency encoding, it causes the precession frequency of the local magnetization to vary linearly along the x-axis.
G_y is responsible for the phase encoding, it is applied for a fixed time interval and creates a phase shift that varies across the y-axis.

The sequence must be repeated, changing the gradients amplitude, to sample entirely the k-space [18, 19, 20].

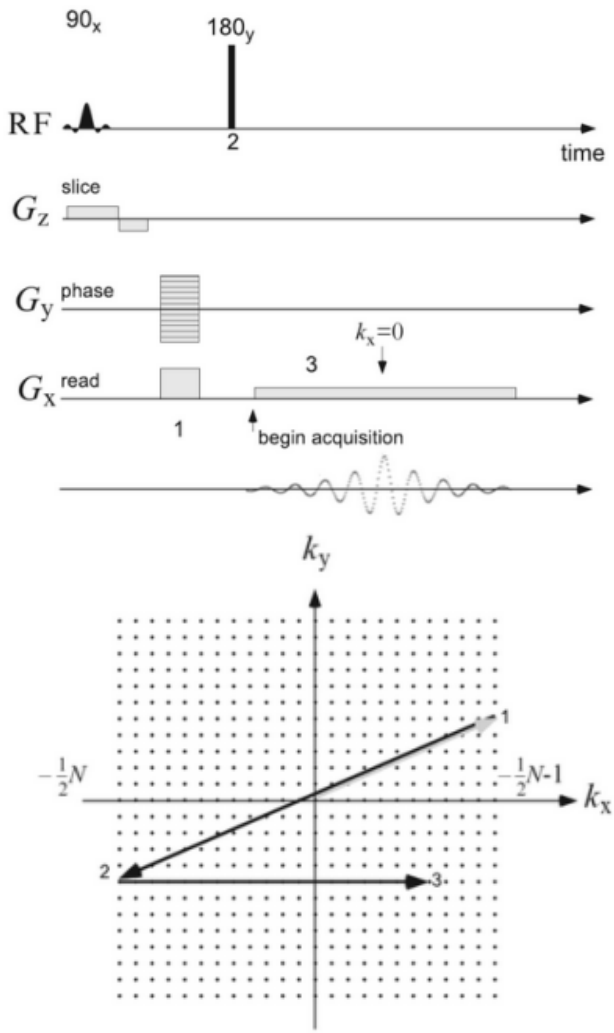

Figure 1.5: *Spin echo sequence with an example of a possible* ***k****-space trajectory. The three steps of the trajectory are explain in the text. [20].*

1.1.2 Tree dimensional reconstruction

The signal acquisition descried so far is an example of two dimensional planar imaging, where only one slice is selectively excited and acquired at each time. With this approach, it is possible to image an entire volume by acquiring many slices in succession.
Three dimensional imaging can be also achieved by eliminating the slice selective pulse and exciting a whole volume or a slab of tissue. In this technique, the spatial information in the third dimension z is encoded by phase encoding the z-axis in addition to the y-axis. Therefore, data must be collected for every possible pairing of phase-encoding steps in y and z, such as for each phase encoding in y, the full range of phase-encoding steps in z must be acquired. Compared to the two dimensional reconstruction, with this method the acquisition time increases with the number of phase-encoding in the z-direction, making the scanning time prohibitively long.
However, by using a gradient echo (GRE) sequence, whose TR can be less than 10 ms, it is possible to image an entire volume with high resolution in few minutes.
The main benefit of the three-dimensional acquisition is a large enhancement in the SNR. Indeed, the image SNR depends on the voxel volume, determining the contribution of the signal in that voxel, and the root square of the number of signal measurements as $\Delta V\sqrt{n}$. In two-dimensional acquisition, n is given by the n_x samples collected during frequency encoding every n_y phase encoding steps, $n = n_x n_y$, whereas in the three-dimensional method the signal from each voxel contributes to every measurement, $n = n_x n_y n_z$, resulting in an improvement of the SNR compared to classical two dimensional reconstruction.

1.1.3 Pulse sequences

The versatility of MRI lies in the fact that the measured signal depends on several tissue properties and the image contrast can be varied depending on the sequence parameters. This makes MRI a unique imaging tool, considerably different from other

types of radiological imaging. In MRI technique the image is a map of the local transverse magnetization of the hydrogen nuclei, a process that depends on several intrinsic tissue properties.
Since the invention of MRI, a plethora of different pulse sequences have been designed in order to investigate different tissue features and provide different image contrasts.
In this work, two different pulse sequences have been used: the pulsed gradient spin-echo to perform diffusion imaging and the gradient echo to perform the rotating frame relaxation imaging.

The Spin-Echo pulse sequence An *echo* signal is based on the dephasing of transverse magnetization, caused by magnetic field inhomogeneity. In 1950, Erwin Hahn [38] found that this loss of phase coherence can be reverted. The reversion is accomplished by applying a 180° pulse after the first RF pulse.

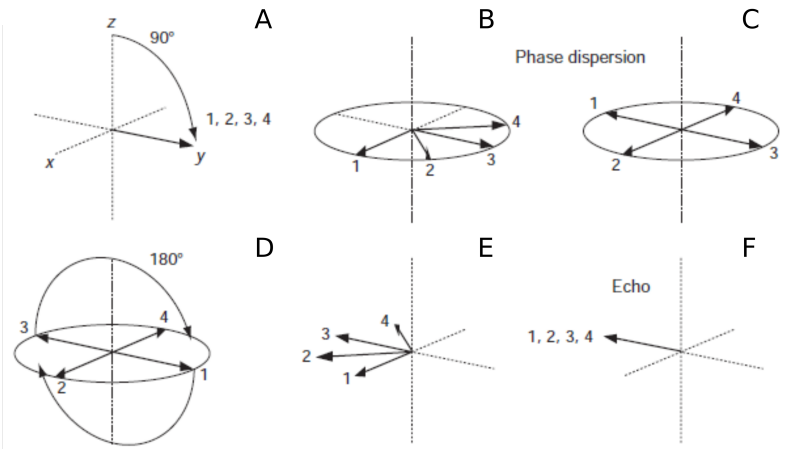

Figure 1.6: *Schematic representation of the formation of an echo signal [18].*

The 90° pulse generates a phase coherence along the y-axis (Fig. 1.6 A) that disappears because of T_2^*-relaxation (Fig. 1.6 B-C), i.e. the field inhomogeneities, creating a FID that decays away very quickly.

Besides the intrinsic T_2 relaxation, field inhomogeneity causes spins to acquire different phases $\phi(\boldsymbol{r})$ depending on their spatial position, $\phi(\boldsymbol{r}) = \gamma \Delta B_0(\boldsymbol{r}) TE/2$.
After the delay $TE/2$, a 180° pulse rotates all magnetization vectors about y by 180° (Fig. 1.6 D), inverting the sign of the phase. The second RF pulse refocuses the spins along the y-axis to create the spin-echo signal at the echo time TE (Fig. 1.6 E-F).
The spin-echo imaging is realized by adding imaging gradients for each spatial direction to space-encode the acquired signal as described in the previous section.

The Gradient-Echo sequence A gradient echo (GRE) signal can be produced by applying a RF pulse followed by a negative gradient. For the duration of the gradient, spins at different positions along the gradient axis will precess at different rates, generating a phase dispersion, which grows during the application of the gradient, and a reduction of the net signal. However, if an opposite gradient pulse is applied for the same duration, it will reverse the phase of each spin, decreasing the phase dispersion until all the spins are coherently in phase again, producing a strong gradient echo signal that is collected during the read-out (Fig. 1.7).
Similarly to the spin-echo, the gradient-echo imaging is realized by adding imaging gradients

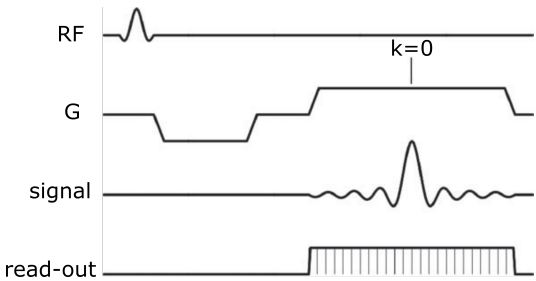

Figure 1.7: *Schematic representation of the formation of an echo signal [18].*

1.2 Diffusion MRI

Diffusion is that chaotic and uncontrollable process described for the first time by Lucretius in *De rerum Natura* as prove of the atomic nature of matter.
Since its first scientific description given by Brown in 1827, the phenomenon of diffusion found its most powerful mathematical formulation with the Einstein relation $D = \mu k_B T$, a simple equation that links the diffusion coefficient D to dynamic (the mobility μ), statistical mechanic (the Boltzmann's constant k_B) and thermodynamic (temperature T).
In 1965 Stajslak and Tanner found a way to exploit the physiological and thermally-driven diffusion motion of water molecules in living tissue as an endogenous contrast to perform imaging [86].
The simple idea was to make the MR signal sensitive to the diffusion of water molecules by using two additive gradient pulses, with a pulsed gradient spin echo sequence (PGSE).
In Diffusion MRI the molecular diffusion is measured from the attenuation of the spin echo signal which occurs from the dephasing generated by the motion.

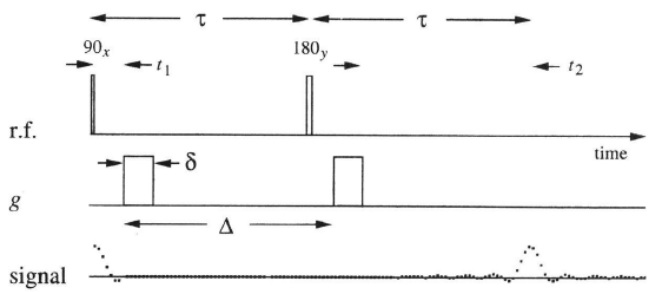

Figure 1.8: *Pulsed gradient spin echo sequence (PGSE), with gradient magnitude g and duration δ and gradient time spacing Δ; the pulsed gradients are applied before and after the* 180° *pulse [20].*

The motion encoding is possible by applying two pulsed gradients with same magnitude g, duration δ and with a time separation of Δ. The effect of the second gradient consists in balancing the dephasing due to the first gradient. During the time interval Δ, diffusion process causes the spins to experience different local field gradients, generating an additional dephasing, further to the one created by the the first pulsed gradient.
Then, if the spins diffuse, the effects of the first pulse will not totally be balanced by the second one and each spin will be left with a small random phase offset $\Delta\phi = \gamma g \delta \Delta x$ that depends on the distance travelled by diffusion $\Delta x = \boldsymbol{r}_0 - \boldsymbol{r}_1$ during the interval Δ [20].

$$\frac{S(t, \Delta\phi)}{S(t, 0)} = \iint \rho(\boldsymbol{r}_0) P(\boldsymbol{r}_0, \boldsymbol{r}_1, \Delta) e^{i\Delta\phi(\boldsymbol{r}_0 - \boldsymbol{r}_1)} d\boldsymbol{r}_0 d\boldsymbol{r}_1, \tag{1.13}$$

where $P(\boldsymbol{r}_0, \boldsymbol{r}_1, \Delta)$ is the diffusion propagator, representing the probability density that a spin moves from r_0 to r_1 during Δ over all possible starting and finishing positions.
This equation represents a key relation in the diffusion NMR technique, connecting the diffusion process and the NMR signal. Equation 1.13 states that the acquired signal is equal to the Fourier Transform of the average motion propagator. In the case of isotropic free diffusion, the mean propagator is Gaussian shaped and by solving the integral in Eq. 1.13, we find the PGSE signal attenuation for isotropic free diffusion, called also the Stejskal-Tanner equation [80]:

$$\frac{S(g)}{S(0)} = e^{-(\gamma g \delta)^2 (\Delta - \frac{\delta}{3}) D} = e^{-bD} \tag{1.14}$$

where D is the diffusion coefficient, $b = (\gamma g \delta)^2 (\Delta - \frac{\delta}{3})$ is the *b-value*, that depends on the gyromagnetic ratio γ, the gradient strength g, the gradient duration δ and the temporal distance between the two diffusion gradient pulses Δ, while $S(0)$ is the signal with no gradients applied ($b = 0$). The b-value represents the diffusion weighting and can be varied by changing the gradient strength g and/or the diffusion time Δ.

An estimation of the diffusion coefficient D, also called the *apparent diffusion coefficient* (ADC), is possible by measuring the echo signal at different b-values and fitting the logarithm of the signal intensity $\ln(S(g)/S(0))$ on varying the b-value.
The image obtained by the PGSE signal is called Diffusion Weighted Image (DWI) and represents the displacement distribution of water molecules within the tissue.

1.2.1 Diffusion tensor

In the previous sections we found that in a MRI experiment the effect of diffusion on the echo signal is an attenuation, which depends on the diffusion coefficient D and on the *b-value*.
The diffusion coefficient completely describes the diffusion process and it can be evaluated at each voxel by fitting the received signal intensity at different b-values with the Eq. (1.14).
If the diffusion is anisotropic, the diffusion coefficient it is no longer a scalar, but rather a symmetric tensor and the signal attenuation becomes:

$$\frac{S(g)}{S(0)} = e^{-\sum_{i,j=1}^{3} b_{ij} D_{ij}} \tag{1.15}$$

Since the diffusion tensor is symmetric, a fully determination of it is obtained with a series of DWIs along almost six gradient directions in addition with an image without diffusion weighting. Generally, the estimation of the diffusion tensor is achieved with a multiple linear regression.
By diagonalizing the diffusion tensor, it is possible to calculate eigenvectors and eigenvalues in each voxel, which respectively represent the principal directions and values of diffusivity.

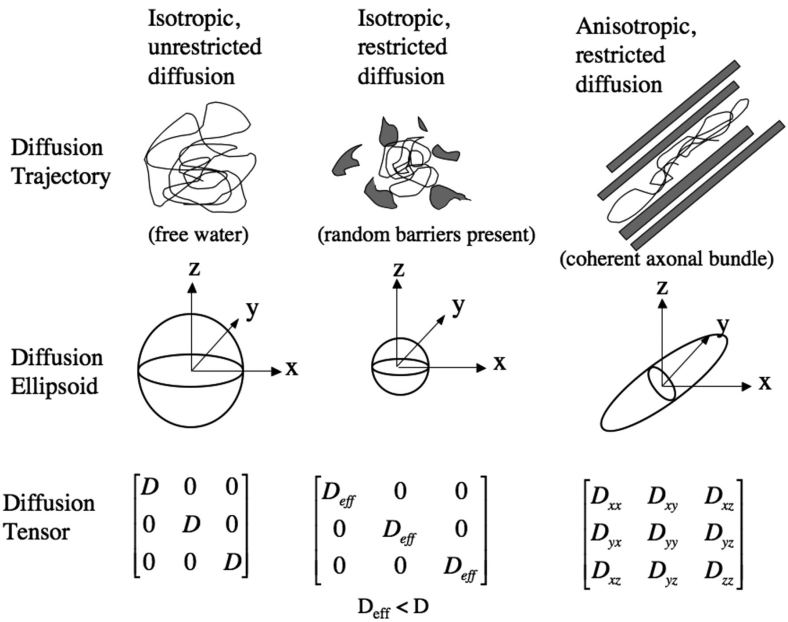

Figure 1.9: *The diffusion tensor and its ellipsoidal representation are showed for the case of isotropic free and restricted diffusion and for anisotropic restricted diffusion [71].*

The diffusion tensor can be visualized as an ellipsoid (Fig. 1.9), whose main axis identifies the main diffusion direction within the voxel and its eccentricity describes the degree of anisotropy [77]. When the diffusion is isotropic, as in a compartment of free water, the diffusion coefficient is a scalar and is represented by a sphere (Fig. 1.9, first column). In presence of obstacle homogeneously distributed, the diffusion coefficient is still a scalar, but represented by a sphere with a smaller radius (Fig. 1.9, second column). Instead, when the diffusion occurs in anisotropic compartments that exhibit a preferential diffusion direction, such as the brain axons or the prostate stroma, the diffusion coefficient is a tensor, described by an oblate or prolate ellipsoid (Fig. 1.9, third column).
Starting from the knowledge of the diffusion tensor, two fundamental parameters for the Diffusion Tensor Imaging (DTI) can

be calculated, *mean diffusivity* and *fractional anisotropy*.
The mean diffusivity (MD) defines the mean-squared displacement of molecules within a voxel and reveals the overall presence of obstacles to diffusion. Essentially, MD is a parameter sensitive to changes in medium viscosity and in cellular size and density and it is calculated as the average of the eigenvalues

$$MD = \frac{\lambda_1 + \lambda_2 + \lambda_3}{3}. \tag{1.16}$$

The fractional anisotropy (FA) quantifies the deviation of the diffusivity from the mean diffusivity in the principal spatial directions

$$FA = \sqrt{\frac{3}{2}} \frac{\sqrt{(\lambda_1 - \widehat{\lambda})^2 + (\lambda_2 - \widehat{\lambda})^2 + (\lambda_3 - \widehat{\lambda})^2}}{\sqrt{\lambda_1^2 + \lambda_2^2 + \lambda_3^2}}, \tag{1.17}$$

where $\widehat{\lambda} = \frac{\lambda_1+\lambda_2+\lambda_3}{3}$.
The value of FA ranges in $[0, 1]$, where 0 characterizes an isotropic diffusivity, while 1 reveals an anisotropic diffusivity, related to the presence of oriented structures.
These quantities are rotational invariant, such as independent of the subject orientation in the magnet or of the laboratory frame. Rather, MD and FA describe the diffusivity in the reference frame of the diffusion itself, that is calculated in each voxel from the diffusion tensor and it is defined by the tissue microstructure in a specific voxel.
The introduction of the parametric maps revolutionised the neuronal diagnostic, providing early diagnosis in several brain diseases [8, 9, 10, 60].
The diffusion tensor model is founded on the assumption that molecular displacements obey Gaussian distribution, a hypothesis that is correct for diffusion processes that occur in free and isotropic media. Nevertheless, diffusion in biologic systems are crowded by cell membranes, fibres and macromolecules, causing a deviation of the diffusion process from the Gaussian behaviour. Therefore, in this work we investigated the feasibility in clinical applications of an imaging technique that takes into account

the presence of non-Gaussian processes, the Diffusion Kurtosis Imaging, discussed in the following section.

1.2.2 Diffusion Kurtosis Imaging

Diffusion kurtosis imaging (DKI) technique provides a representation of NMR signal when diffusion is probed with high b-values. In particular, Kurtosis is the second order term of the DWI-signal (Eq. 1.13) expansion in terms of the b-value [56, 55]:

$$\frac{S(n)}{S_0} = e^{-bD(n)+\frac{1}{6}b^2D(n)^2\cdot K(n)} \tag{1.18}$$

where $K(n)$ is the kurtosis and $D(n)$ the relative apparent diffusion coefficient, both estimated in a given diffusion direction n. As already mentioned, biologic tissues are characterized by a complex and heterogeneous organization of structures and cell membranes which act like natural barrier for water molecules, leading to a restriction of the diffusion motion. In presence of restricted diffusion, the distribution of molecule displacements is no longer Gaussian and the signal decay is no longer a simple mono-exponential (Fig. 1.10). The kurtosis parameter quantifies the deviation of the displacement distribution from a Gaussian shape, or, similarly, the deviation of the DWI signal from the mono-exponential decay (Fig. 1.10). Indeed, in case of free diffusion, the kurtosis term is null and the previous equation reduces to Eq. 1.14.

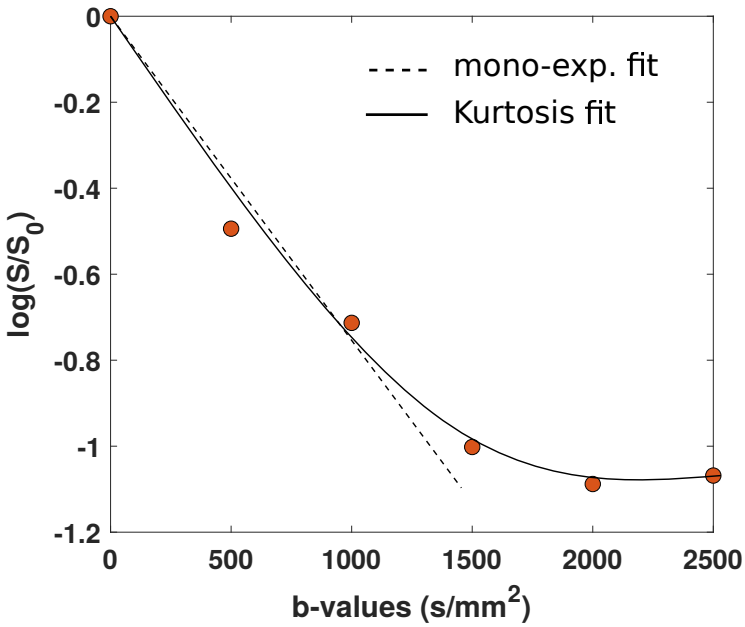

Figure 1.10: *An example of data fitting performed with mono-exponential and kurtosis decay. Data are relative to a pixel in PCa of a randomly chosen subject.*

Since the heterogeneity of the confining structures causes the deviation from the Gaussian behaviour, kurtosis was suggested to provide information on tissue microstructure [49]. In particular, the kurtosis term quantifies diffusion heterogeneity arising from multiple tissue compartments with different diffusion behaviours [49], unveiling additional details on tissue organization, inaccessible to DTI technique.
One limitation of the technique is that the kurtosis equation 1.18 predicts an unlimited growth of the DWI signal with the b-value, implying that DKI can be performed for a limited range of b-values or that higher-order moments have to be considered [36]. However, DKI is a technique suitable for any biologic tissue, since it not requires a priori knowledge of tissue biophysical properties; rather, DKI is a phenomenological description of diffusion NMR

signal in presence of non-Gaussian diffusion processes [49, 73, 75].

1.3 Rotating frame relaxation imaging

Typically, for "relaxation imaging" we refer to the techniques that exploit T_1 and T_2 relaxation processes to provide image contrast, largely employed in clinical imaging.
In this work, we used techniques of *spin-lock* $T_{1\rho}$ and $T_{2\rho}$, which exploit relaxation in the rotating frame, producing a different type of image contrast.
Such relaxation are called $T_{1\rho}$ and $T_{2\rho}$ and they occure during the application of radiofrequency pulse. During *spin-locked* $T_{1\rho}$, magnetization is *locked* along the direction of the effective magnetic field B_{eff} (defined below).
In this work, the spin-lock condition is generated with *adiabatic RF pulses*, that differ from the pulses conventionally used for being both amplitude and frequency modulated, such as their frequency is a function of time [88]. Since the frequency of the adiabatic pulse changes with time, it will deviate from the Larmor frequency, generating "off-resonance effects" as a function of time.
To visualize the dynamic of the magnetization vector let's refer to the first rotating frame (x', y', z'), which rotates around $z'(\equiv z)$ with frequency ω_{RF}. In this frame, B_1 does not precess in the transverse plane, but has a fixed orientation along x' (Fig. 1.11). In addition to B_1, spins experience the presence of a residual magnetic field oriented along z' with magnitude $B_{z'} = B_0 - \omega_{RF}/\gamma$. Consequently, an effective field is generated as

$$B_{eff} = \sqrt{B_1^2(t) + B_{z'}^2}, \tag{1.19}$$

whose orientation is defined by

$$\alpha = \arctan\left[\frac{\gamma B_1}{\omega_0 - \omega_{RF}}\right]. \tag{1.20}$$

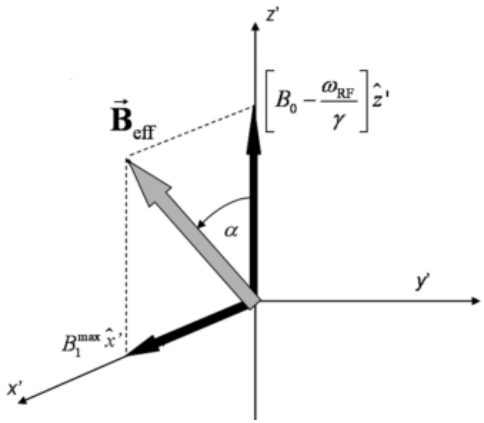

Figure 1.11: Induced B_{eff} in the rotating frame (x', y', z').

When ω_{RF} is time dependent, also $B_{eff}(t)$ and $\alpha(t)$ are time dependent. In particular, the adiabatic condition is satisfied when the angle α precesses slower than the precession frequency, $|d\alpha/dt| \ll \gamma|B_{eff}|$. In this case, the magnetization vector remains *locked* along the orientation of B_{eff}, if magnetization was initially collinear with B_{eff}, while it precesses in a plane perpendicular to B_{eff} if it was initially perpendicular to B_{eff}.
One can picture the dynamic of B_{eff} during the application of the adiabatic pulse considering the Eq. 1.20 as shown in Fig. 1.12. When $\omega_{RF}(t) \ll \omega_0$ at the beginning of the pulse, the ratio in Eq. 1.20 is small and the initial orientation of B_{eff} is approximately parallel to z' (Fig. 1.12A). As $\omega_{RF}(t)$ increases with time, B_{eff} rotates toward the transverse plane, equaling B_1 when $\omega_{RF}(t) = \omega_0$ (Fig. 1.12B). In this way, we generated a 90° excitation through an *adiabatic half-passage*. Similarly, we could achieve a 180° excitation (*adiabatic full-passage*), leading B_{eff} along z' at $\omega_{RF}(t) \gg \omega_0$ [25, 88] (Fig. 1.12c).

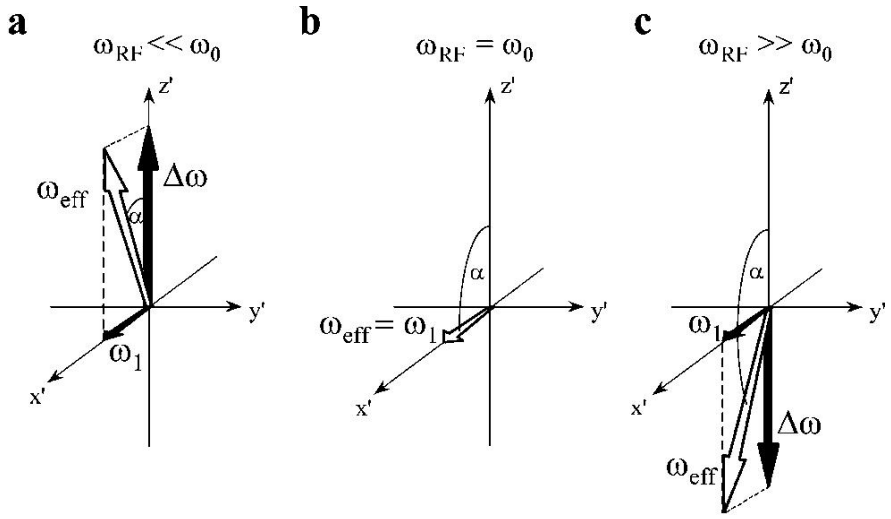

Figure 1.12: Dynamic of B_{eff} during the application of the adiabatic pulse [88].

Typically, one of the disadvantage of the MRI experiments is the inhomogeneity of the excitation field B_1, causing spatial variations in spin flip angles and degrading the sensitivity of the receiver coil. Adiabatic RF excitation overcomes this limit, being insensitive to spatial B_1 inhomogeneities and off-resonances in the sample. Moreover, adiabatic condition can be easily achieved with an arbitrarily low B_1 amplitude and a long duration pulse. In general, designing adiabatic pulses is non trivial, since they are often constructed out of hyperbolic tangent or secant functions, with independent amplitude and frequency modulation.
The relaxation process occurring in the rotating frame when the magnetization is locked along the direction of B_{eff} it is ruled by the relaxation time $T_{1\rho}$, while $T_{2\rho}$ is the relaxation time when the magnetization precesses in a plane perpendicular to the direction of B_{eff}. Therefore, in analogy with the conventional constant time T_1 and T_2 that characterize the magnetization relaxation occurring in the laboratory frame, $T_{1\rho}$ and $T_{2\rho}$ are the longitudinal and transverse relaxation times in the rotating frame.
In the next paragraph we discuss how to obtain images with $T_{1\rho}$

and $T_{2\rho}$ contrasts [65, 68].

$T_{1\rho}$ and $T_{2\rho}$ in biological systems The relaxation time $T_{1\rho}$ is sensitive to magnetic dipolar fluctuations occurring not only at frequencies around ω_0 (typically in the kHz range), but also at frequency around $\omega_{eff} = B_{eff} \cdot \gamma$ [12, 65, 68].
Since ω_{eff} critically depends on the property of the pulse via B_1 and ω_{RF}, the image contrast can be changed by "tuning" the amplitude and frequency modulation functions. This is impractical for the laboratory frame relaxation time T_1 and T_2, whose sensitivity to molecular dipolar interactions is determined uniquely by the Larmor frequency, occurring at higher frequency, typically in the MHz range.
A brief description of the theoretical formalism formulated to describe relaxation due to isochronous exchange in the case of two spin populations is provided in the following, for a more comprehensive description the reader can refer to [65, 68].
Let's consider two spin populations A and B, they could be water and a certain macromolecule, with population density P_A and P_B. The difference in chemical shift between the two populations is $\delta\omega$ and k_1 and k_{-1} represent the forward and backward exchange rate constants defined by the McConnell relationship:

$$\tau_{ex} = \frac{P_A}{k_1} = \frac{P_B}{k_{-1}} \tag{1.21}$$

Since $T_{1\rho}$ and $T_{2\rho}$ are dependent on both the amplitude and frequency modulation of the adiabatic pulses, through $\alpha(t)$ and $\omega_{eff}(t)$, the exchange rates $r_{1\rho} = 1/T_{1\rho}$ and $r_{2\rho} = 1/T_{2\rho}$ during the adiabatic pulse will depend on time:

$$R_{1\rho,ex}(t) = P_A P_B \delta\omega^2 sin^2\alpha \left(\frac{\tau_{ex}}{1 + (\omega_{eff}(t)\tau_{ex})^2} \right) \tag{1.22a}$$

$$R_{2\rho,ex}(t) = P_A P_B \delta\omega^2 cos^2\alpha \tau_{ex}. \tag{1.22b}$$

The previous equations are valid in the fast exchange regime $\tau_{ex} \ll 1/\delta\omega$ [65, 68].

1.3.1 $T_{1\rho}$ and $T_{2\rho}$-weighted imaging

Generally, rotating frame relaxation imaging is achieved with a sequence that includes a magnetization preparation module followed by a readaout (Fig. 1.13A).
To generate $T_{1\rho}$ contrast, a train of AFP pulses is placed before the imaging readout sequence (Fig. 1.13A). For $T_{2\rho}$ contrast instead, the pulse train is enclosed between two adiabatic half passages that flip the magnetization to the transverse plane first and then flip it back to the z'-axis before the readout (Fig. 1.13B).

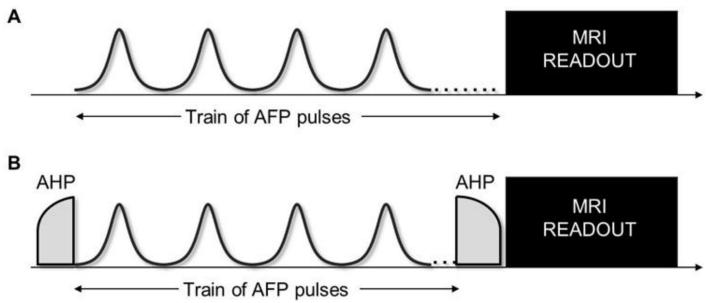

Figure 1.13: Schematic representation of $T_{1\rho}$ (A) and $T_{2\rho}$-weighting (B) imaging sequence [68].

The $T_{1\rho}$- and $T_{2\rho}$-weighting is obtained by increasing the number of pulses in the train, or in other words by increasing the time of spin-lock (TSL) [65, 68].
During the spin-lock, the longitudinal and transverse magnetization in the rotating frame experiences exponential decay, which is generally approximated as a mono-exponential decay:

$$\mathbf{M}(t) = M_0 e^{-TSL/T_{1,2\rho}}, \tag{1.23}$$

where M_0 represents the magnetization at the beginning of the magnetization preparation.
In the present study, the $T_{1\rho}$ or $T_{2\rho}$ prepared magnetization was imaged with a 3D gradient echo (GRE) to reduce the acquisition time and improve the SNR.

Chapter 2

Conventional and novel approaches for prostate cancer MRI

Prostate cancer (PCa) is one of the most common cancer in Western countries, second only to lung and bronchus cancer in mortality and the most frequently malignancy diagnosed among men aged > 45 [40].
Given the high incidence of PCa and the limitations of current diagnostic methods, the aim of this work is to test the potential ability of NMR diffusion parameters to improve PCa diagnosis protocols. For this purpose, it is necessary to introduce a brief description of the prostate glandular structure and the grading system of PCa.

2.1 Essentials of prostate anatomy

The prostate is an exocrine gland that surrounds the urethra at the neck of the urinary bladder. It can be divided into three major zones: central, transition and peripheral zone.
The *peripheral zone* (PZ) is located in the back of the prostate gland closest to the rectum. It is the largest zone of the prostate gland and is the site of about 80% of prostate cancer.

The *transition zone* (TZ) is sited between the peripheral and central zone and it makes up about the 5% of gland volume.
The *central gland* (CG) is the farthest part from the rectum and represents about the 25% of the gland.
The prostate tissue consists in $30 - 50$ glands surrounded by fibromuscolar stroma; each gland is made by acini, that encircle the lumen, and ducts.
The stroma consists of dense connective tissue and bundle of muscle cells and it thickens in the central zone. The connective tissue is made up of collagen fibre with $1 - 2\mu m$ of diameter.
In normal prostatic tissue, glands are well-defined, separated and approximately with same size and shape; while, cancer tissue appears irregular, with glands progressively change size and shape depending on tumour grade [79].

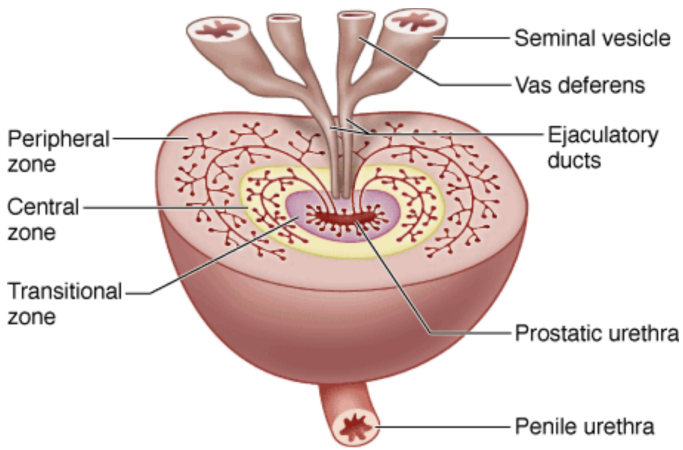

2.1.1 Gleason grading system

The evaluation of tumour grade is based on microscopic observation of prostate tissue section, obtained by biopsy.
Carcinoma histological patterns are compared with Gleason grades, each of which represents a degree of cells differentiation.
The Gleason grading system, developed by the pathologist Dr.

Donald F. Gleason, is based upon five basic grade patterns, each of which is scored with a number from 1 to 5. These patterns are illustrated in a standard drawing (Figure 2.1), used as a guide by pathologists to identify the specific Gleason grades.
The five basic patterns are used to generate a score, from 2 to 10, by adding the grades related to the two most common patterns observed. If only one pattern is present in the sample, the score is given by multiplying that grade by two.
Gleason grade is directly related to several histopathological features, such as tumor size, margin status of glands, and pathological stage. The aim of this work is to find among the different NMR diffusion parameters those or that capable to discriminate between healthy and PCa tissue and suited to correlate with Gleason score, providing a correct and mostly non-invasive diagnosis.
Understanding carcinoma pattern arrangement is useful to realize water diffusion in prostate tissue; in fact, given the inhomogeneous tissue structure, different water diffusion behaviours can be observed: highly restricted diffusion in the epithelial cell layer, moderately restricted diffusion in the stroma, and relatively free diffusion in the gland lumen and ducts.
Therefore, it would be necessary to distinguish different diffusion behaviors, relative to different compartments of the prostate anatomy.
A more clear representation of the tumour grades is given by the following figure (2.2), where the Gleason patterns are illustrated both on a macroscopic and microscopic scale. This figure shows how stromal area increases passing from the first (A, F) to the third (C, H) grade, while acinar cells grow, decreasing lumen size; as a consequence, water molecules diffusion is reduced. The fourth (D, I) and fifth (E, L) grade are distinguished by the presence of infiltrating cells that invade stroma, lumen and ducts, ruining the glandular structure of the prostate; thus, the water diffusion becomes highly restricted in these patterns.

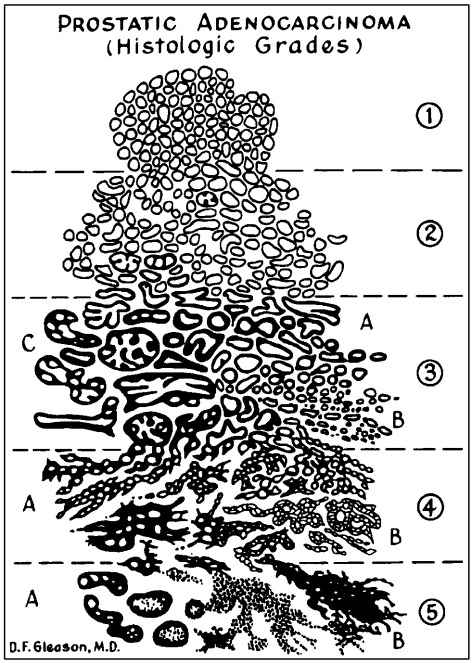

Figure 2.1: *A schematic representation of the five Gleason grade. 1) The first grade is the rarest, shows a well-differentiated carcinoma with small, well-formed and closely packed glands. 2) In second grade glands are still well-formed, but with variable size and shape and enhanced glands separation. 3) The third, the most common pattern, shows an increase of stromal separation of glands, usually greater than one gland diameter. 4) In the fourth grade glands appear with ragged edges, many cells invading stroma, presenting a very poorly cell differentiation. 5) The fifth is the most unwell-differentiated pattern, with unrecognizable glands and highly infiltrating cells. [45].*

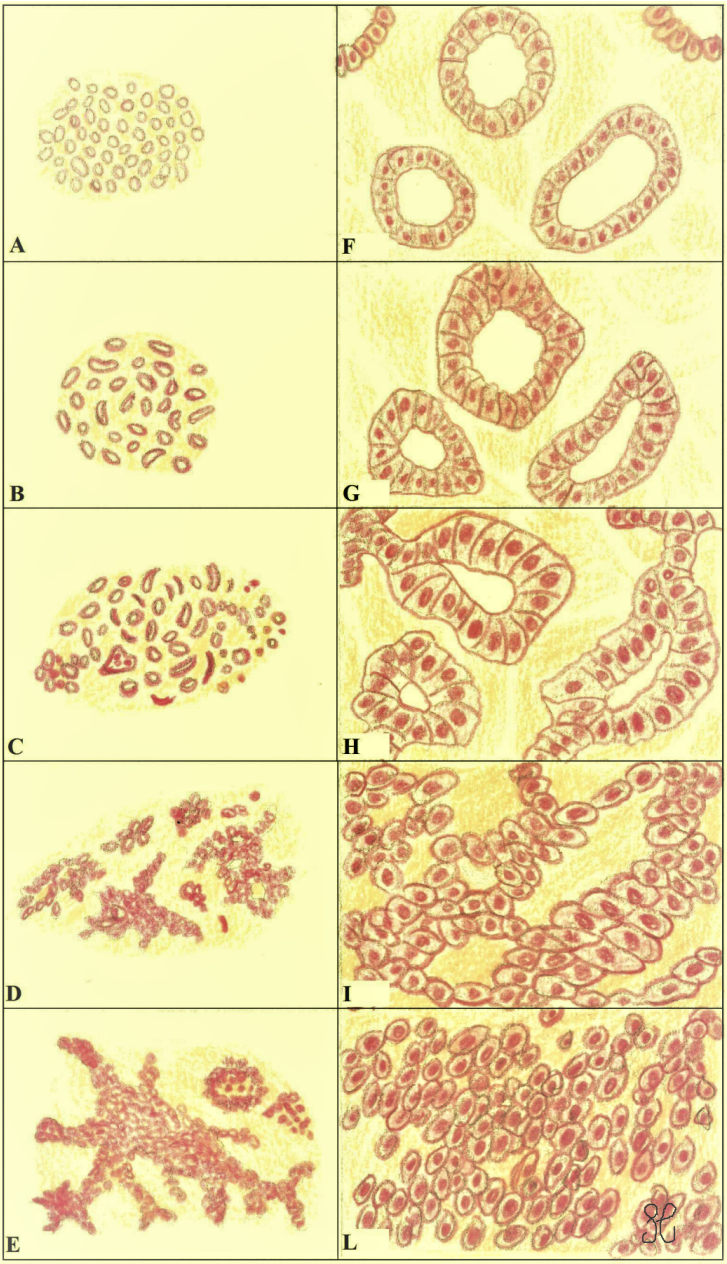

Figure 2.2: *A representation of the basic Gleason grade patterns on a macroscopic scale on the left (A→E). For each grade an illustration of the prostatic tissue at microscopic level is reported on the right (F→L).*

2.1.2 Limits of PCa detection

Clinical treatment of prostate cancer depends on clinical stage, Gleason score, PSA levels and patient age. The evaluation of these variables is finalized to stratify patients into low (GS<3+3), intermediate (GS=3+3, 3+4), and high-risk (GS≥4+3) groups, according to the recent work of Epstein et al. [28].
In this work, tumours were graded according the system recently proposed by the International Society of Urological Pathology (ISUP) [76, 28], which was proven to be more accurate in predicting PCa progression and in reflecting PCa biology. The ISUP grading system consists of five distinct GG, related to the GS as follows GG1=GS6, GG2=GS3+4=7, GG3=GS4+3=7, GG4=GS4+4=8, GG5=GS9 and GS10.
Since several studies showed that GS4+3=7 demonstrates worse pathological stage and biochemical recurrence rates than GS3+4=7 [22, 53], we consider GG≤2 (GS≤3+4) and GG≥3 (GS≥4+3) as low- and high-risk prostate cancer, respectively. The importance of a correct identification of cancer state lies in guaranteeing the adequate treatment. In fact, low-risk cancer requests an active surveillance, that consists in monitoring the course of disease. The treatment of cancer with GS=3+3,3+4 and GS≥4+3 is radically different: active surveillance focal therapy and pharmacological treatment is recommended in the first case, while in the second case invasive treatments are necessary, as radiotherapy and radical prostatectomy. Since current surgical procedures cannot provide an accurate localization of tumour area, these invasive treatments are directed to the entire gland, and potentially they can damage neighbouring structures, resulting in disabling complications, such as urinary incontinence and erectile dysfunction.
To succeed in differentiating intermediate- and high-risk cancer, it is fundamental to avoid unnecessary invasive treatment: this is one of the aims of this work.
Early detection of PCa consists in finding elevated PSA level or abnormality during DRE, although neither of the two tests is accurate [70].

In clinical screening a PSA level of $4.0 ng/ml$ is considered normal [4]; however, men with normal PSA have prostate cancer in 15% of cases and even high-grade cancer in 2% [70].
An increasing of the PSA level can be connected to several benign factors, besides cancer [24],

- Benign prostatic hyperplasia (BPH), a non-cancerous enlargement of the prostate;
- Prostatitis, an inflammation of the prostate gland;
- Aging, PSA level normally raises in older age.

Since benign conditions can cause elevated PSA levels, PSA measurement has low specificity (36%) [70]; thus a normal PSA can't exclude a tumour suspicion and increased PSA is not necessary indicative of cancer.
Definitive diagnosis requires biopsy of the prostate, usually performed under transrectal ultrasound guidance.
Biopsy consists in the removal of a tissue sample using a needle; usually, urologists repeat the procedure even 18 times to take about 12 samples. The procedure is accomplished following a systematic scheme of sampling, represented in Figure 2.3. Biopsy

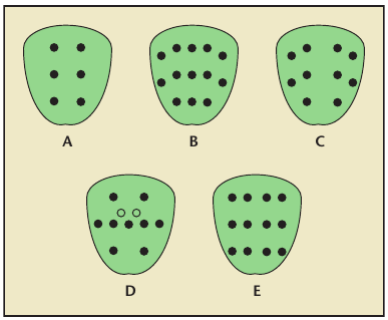

Figure 2.3: *Examples of biopsy schemes in coronal plane [79].*

is the only test that can provide information on tumour grade, but false-negative results are common. A simple explanation of that can be given considering that the specimen extracted in a

biopsy test is approximately 1% of the entire prostate gland and it can be localized in a non-cancerous region. The probability of missing a cancer by biopsy is estimated at about 25%, then a repeated biopsy is necessary if the suspicion of prostate cancer persists.
Moreover, in 85% of cases, prostate cancer is multi-focal and with biopsy the effective extension and grade of tumour may be underestimated [72]. In fact, it is not uncommon (30% of cases) that, what appeared like a low-grade disease, results upgraded in Gleason score after prostatectomy [31].
Generally, prostate biopsy is a safe procedure, but it can lead to several complications [63].
Thus, biopsy involves considerable physical and psychological suffering for patients and it is also affected by both procedural limitations, as sampling errors and missing of cancer areas, and diagnostic limitations, as underestimation of Gleason score and tumour extension.
An improvement of clinical procedures involved in PCa diagnosis seems indispensable and it is exactly what I tried to accomplish in this work: to provide a way to go beyond the above-mentioned techniques limitations using the diffusion MRI.

2.2 Experimental design: materials and methods

This section refers to the scientific methods employed to study prostate cancer with different MRI techniques.
The first subsection concerns the high-resolution experiments carried-out ex-vivo on normal and cancer human prostate samples, obtained by radical prostatectomy surgery. In the following two subsections, we investigated the diagnostic ability of DTI and DKI, respectively, in individuating and classifying PCa on human subjects with biopsy-proven prostate cancer.
These in-vivo studies initially included 68 patients who under-

went the MRI examination between February 2015 and March 2016 at the Tor Vergata Hospital, giving their informed consent. Twenty subjects were discarded from the analysis because biopsy resulted negative in 9 cases and images presented incorrigible artifacts in 11 cases. DTI analysis was conducted on 38 patients, while DKI on 48 patients, since DKI was performed one year later and more patients underwent MRI.
These studies were conducted retrospectively in collaboration with the Tor Vergata Hospital. Patients underwent MRI scan, biopsy and, in some cases, radical prostatectomy regardless of this study, according to the standard urogenital radiology clinical routine, following the European Society of Urogenital Radiology guidelines.
The fourth paragraph concerns the experiments conducted at the CMRR of Minneapolis to investigate the feasibility of $T_{1\rho}$, $T_{2\rho}$ imaging of prostate cancer with a fast acquisition technique on healthy volunteers and on patients with diagnosed PCa, giving their informed consent.

2.2.1 Micro-imaging of DTI and DKI at 9.4 Tesla ex-vivo

Tissue samples were obtained from radical prostatectomy surgery and kept in 4% formaldehyde solution in phosphate buffered saline (PBS) at 4°C. An expert uropathologist selected one normal and one cancer sample from 3 patients with high-grade Pca (Gleason Score $\geq$ 4+4).
ROIs were manually drawn in stroma, PCa and normal tissue with the supervision of the uro-pathologist.

Imaging protocol Image acquisition was performed with a 9.4T micro-imaging scanner (Bruker AV400 spectrometer) at the CNR-ISC Segré Laboratory of the Sapienza University. The scanner was equipped with a micro-imaging probe (10mm internal maximum diameter) and maximum gradient strength of 1200

mT/m. XWINNMR and ParaVision 3.0 software were employed for data acquisition.
DWI was performed with a Pulsed Gradient Stimulated Echo (PGSE) by varying diffusion gradient strengths, more details in Table 2.1. Five non-zeros b-values were acquired along 6 non-collinear directions, as reported in Table 2.1.

Table 2.1: Acquisition parameters for the micro-imaging protocol.

PGSE	
b-values	0,500,1000,1500, 2000,2500 s/mm^2
Repetition Time	4500 ms
Echo Time	14,8 ms
Field of View	150x130x70 mm^3
Pixel dim.	70x70 μm
Slice thickness	1 mm
δ/Δ	3/40 ms
Signal averages	8
Diffusion Directions	6

Diffusion parameter estimation DTI was performed by using FSL 5.0 software, with b-value range 0-1500 s/mm^2.
Apparent mean kurtosis (K), kurtosis-derived diffusion coefficient (D) and proxy Kurtosis Fractional Anisotropy (KFA) were calculated as described in the section 2.2.3, with b-value range 0-2500 s/mm^2.

2.2.2 DTI applications in-vivo

Imaging protocol Image acquisitions were performed at the Tor Vergata Hospital, using a 3 Tesla clinical MRI scanner (Intera

Achieva, Philips Medical Systems, The Netherlands). Patients were examined in supine position with a six-channel receiving coil (SENSE torso) placed at the pubic symphysis.
Our experimental diffusion protocol consisted of a Spin-Echo echo planar imaging with 5 non-zeros b-values, acquired along 6 diffusion directions, in approximately 9 minutes of acquisition. A more detailed description of the acquisition parameters is reported in table 2.2

Table 2.2: Acquisition parameters of the Diffusion protocol

Spin-Echo EPI	
b-values	0,500,1000,1500 2000,2500 s/mm^2
Repetition Time	3000 ms
Echo Time	67 ms
Field of View	150x130x70 mm^3
Pixel dim.	1.56x1.56 mm^2
Slice thickness	3 mm
Gap	0
Signal averages	4
Diffusion Directions	6
Acquisition Time	9 min

T2-weighted images (T2WIs) were used as anatomical and morphological reference to determine biopsy zones and as DTI reference image.

Biopsy Patients underwent the biopsy examination in a period of 1 day-2 weeks after the MRI by expert urologists of the Tor Vergata Hospital. T_2-weighted images were used to contour and record lesion locations. The biopsy was performed in two consecutive sections: first a targeted MR/ultrasound fusion biopsy (BiopSee, Medcom, Darmstadt, Germany) was performed and 2 to 4 biopsy cores were obtained from the targets, followed by a 12

cores transperineal biopsy (sextant and laterally directed biopsies at base, mid-gland and apex). Each biopsy session was performed by different physicians, unaware of the MR findings. Hereafter, histopathological examination was performed and reviewed for each specimen on the basis of the recommendations of the the 2014 International Society of Urological Pathology (ISUP) Consensus Conference [28].

Image pre-processing Images were co-registered and corrected for motion artifacts to minimize voxel misalignment caused by respiratory movements.
The image pre-processing was performed with FSL 5.0 software (FMRIB Software Library v5.0, FMRIB, Oxford, UK) [48]. The DWIs were realigned to the b0-volume with a 2D registration modality, carried out slice-by-slice, through a rigid-body transformation with 3 degrees of freedom and a cross correlation cost function, by using the FMRIB's Linear Image Registration Tool (FLIRT). Since the image contrast changes considerably as increasing b-values, especially for b $\geq$ 1500 s/mm^2, then DWIs at b = 500, 1000 s/mm^2 were realigned to the b0 and DWIs at b = 1500, 2000, 2500 s/mm^2 were realigned to the b = 1000 s/mm^2, in order to improve the accuracy of the registration. The goodness of the co-registration was assessed by calculating the *mutual information* as similarity measure for each realigned slice and DW-image.
Regions of interest (ROI) were manually drawn on the b0-images by referring to T2WIs in the tumor area and in the normal tissue of the contralateral lobe. Tumor lesions were determined as hypointense foci on T2WIs and restricted diffusion areas on DWI by two experienced uro-radiologists along with a physicist expert in the images treatment, blinded to the patient information. Calcifications, necrosis and neurovascular bundles were carefully excluded.
Finally, SNR was calculated in both PCa and normal tissue, as $SNR = mean(signal)/sd(noise)$, considering the internal obtu-

rator muscle as background signal.

DTI parameter estimation The diffusion parameters MD and FA were estimated from the diffusion tensor eigenvalues as described in Section 1.2.1.
The fitting procedure was carried out with DTIFIT tool of FSL [48] by using three different b-value ranges (s/mm^2):

a) 0, 500, 1000

b) 0, 500, 1000, 1500

c) 0, 500, 1000, 1500, 2000, 2500

Mean and standard deviation (SD) of the DTI parameters were computed with a custom-made MATLAB script (MATLAB R2012b, The Mathworks, Natick, MA) within the selected ROIs.

Statistical analysis For each b-values ranges (a, b and c) we used a paired t-test to assess the differences in MD and FA between:

- lesions in TZ and PZ
- benign and PCa tissue

An unbalanced analysis of variance (ANOVA) was used to determine the differences of MD and FA between GG1-2 and GG$\geq$3 and between benign prostatic tissue and GG1-2. Receiver Operator Characteristic (ROC) analysis was used to assess the diagnostic performances of diffusion parameters in discriminating GG1-2 vs.GG3 and GG1-2 vs. GG$\geq$3. Sensibility, specificity, area under curve (AUC) and accuracy were calculated. The best cut-off value was evaluated as the value that maximizes the Youden index (Sensitivity+Specificity-1).
Finally, the correlation between DTI measures and GS was tested with the Pearson's test. P-value $p \leq 0.05$ was considered statistically significant.

2.2.3 DKI applications in-vivo

The image acquisition and the biopsy examination were performed as detailed in the previous section. Before performing the motion correction, as describe above, DWI were corrected for noise and Gibbs-ringing artifacts, by using *dwidenoise* [93] and *unring* [54] tools, respectively.
DTI parameters were estimated with DTIFIT by using b-values = 0, 500, 1000 s/mm^2.

DKI parameter estimation DKI metrics were obtained by fitting DWI signal (S) along each diffusion direction to the equation 1.18.
The estimate of the kurtosis tensor requires each b-value to be acquired at least with 15 gradient directions[49], considerably increasing the scanning time.
Our DWI protocol was designed to be feasible in a conventional clinical protocol, which necessitate a reasonable scanning time.
Therefore, to keep our DWI protocol shorter than 10min, DWI images were acquired only along 6 directions, therefore, the Kurtosis tensor could not be estimated.
Alternately, we estimated $K(n)$ and $D(n)$ for each encoding direction; then, maps of mean apparent kurtosis (K) and mean apparent diffusion coefficient (D) were calculated by averaging over the six diffusion gradient directions, as follows:

$$K = \frac{1}{6}\sum_{i=1}^{6} K(n_i) \qquad D = \frac{1}{6}\sum_{i=1}^{6} D(n_i) \tag{2.1}$$

The fitting procedure, developed in Matlab, performed a pixel-by-pixel nonlinear least-squares analysis, using a trust-region-reflective algorithm.
Moreover, parametric maps of proxy kurtosis fractional anisotropy (KFA) were calculated as proposed by Hansen et al. [41]:

$$KFA = \frac{SD(K(n))}{RMS(K(n))} \tag{2.2}$$

where *SD* indicates the standard deviation, *RMS* the root-mean-square value and n the diffusion gradient directions.
Parametric maps of DKI and DTI metrics were obtained for the entire cohort of patients.
Since cancer tissue could include normal tissue, calculating the mean of diffusion parameters in ROIs may not be the best quantification of diffusion metrics in PCa. For this reason, we performed histogram analysis [50], by measuring, in addition to the mean (m) and the standard deviation (sd), the 10^{th} (p10), 25^{th} (p25) and 90^{th} (p90) percentile of the distribution, i.e. the histogram, of diffusion parameters measured in ROIs. The percentile of a distribution indicates the value below which a given percentage of observations falls: in our case, the 10^{th}, 25^{th} and 90^{th} percentiles represent the values below which the 10%, 25% and 90% of the measures lie, as indicated in Fig. 2.4.
Eventually, we estimated the SNR in both PCa and normal tissue, as reported in 2.2.2.

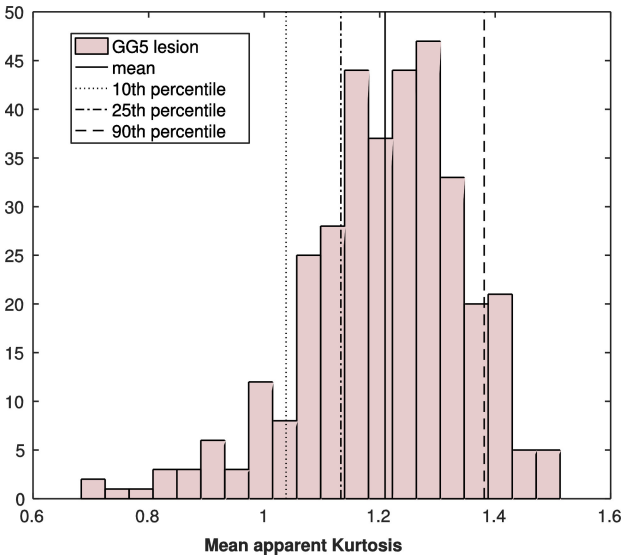

Figure 2.4: *The histogram-derived metrics (mean, 10^{th}, 25^{th}, and 90^{th} percentile) were pointed out in the histogram of K, measured in the entire PCa-ROI of a representative subject with a GG5 lesion.*

Statistical analysis Kolmogorov-Smirnov test was used to assess whether data were normally distributed. When the hypothesis of normality was not satisfied, non-parametric tests were used. Kruskal-Wallis test with Bonferroni correction was carried out to assess statistical significance of differences in each diffusion parameter between PCa, benign and PT tissue.
The correlation between diffusion parameters and GG and the cross-correlations between DTI and DKI metrics in benign, low- and high-GG tissues were assessed with Spearman's and Pearson's correlation test, respectively.
Finally, the ROC curve analysis was carried out to investigate the diagnostic ability of each diffusion parameter in distinguishing low- and high-grade tumours. A p-value $p \leq 0.05$ was considered as statistically significant.

2.2.4 $T_{1\rho}$ and $T_{2\rho}$ applications in-vivo

Prior to perform the experiment on human subjects, our sequences were tested on a anthropomorphic prostate phantom, aiming at designing the optimal protocol with a good image resolution and SNR in a short acquisition time.
The phantom was filled with loading solution to simulate body loading and coil performance. The inner part consisted in 3 rings, targeting a different imaging parameter, i.e. T_1, T_2 and diffusion (Fig. 2.5). The phantom was designed [1] to accomodate the use of ERC and surface coil.
Preliminary tests were conducted on 4 healthy subjects (age range: 27-44y) with surface coil and 1 healthy subject (age: 74y) with ERC coil to compare the 3D acquisition read-out with the 2D, in order to assess the reliability of parameters obtained with the 3D acquisition approach and to measure the SNR.

[1] "Body Phantom with Prostate Mimic for Evaluation of Quantitative MRI". Authors: Ryan M Kalmoe (Imaging Standards Division, High Precision Devices, Inc., Boulder, CO, United States), Elizabeth Mirowski and Gregory J Metzger (Center for Magnetic Resonance Research and Department of Radiology, University of Minnesota, Minneapolis, MN, United States)

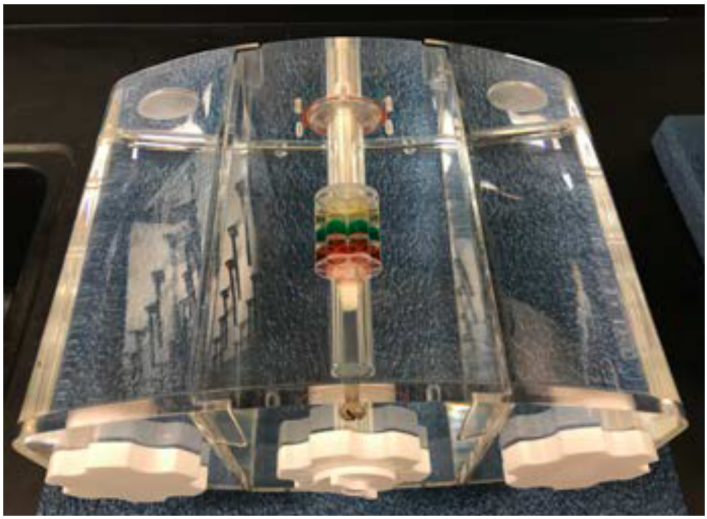

Figure 2.5: *Anthropomorphic prostate phantom* [1].

Imaging protocol Six healthy volunteer (age range: 27-74y) underwent MRI examination on a 3T scanner (Siemens MAGNETOM Prisma) at the CMRR of Minneapolis, giving their informed consent. The experimental protocol consisted of a 3D Gradient Echo readout, preceded by a train of TSL = 0, 4, 8, 12, 16 adiabatic HS1 pulses (more details in Table 2.3). The choice of the image geometry (resolution, slice thickness, number of slices) was made to be comparable to the standard acquisition of the clinical protocol performed at the CMRR.
$T_{1\rho}$ and $T_{2\rho}$-weighted imaging was repeated four times for each subject; between repeated acquisitions each subject was getting off from the scanner. For each relaxation time we acquired 5 volumes and 22 slices in 5.04min. An axial high-resolution T_2-weighted image was acquired as reference for the ROI identification (TR/TE=6000/103 ms, pix. dim. 0.5x0.5 mm, slice thickness 3 mm, num. of slices 22, acquisition time = 2.2min). DWI was also performed with single-shot echo-planar imaging (EPI) combined with reduced volume excitation (ZOOMit; Siemens Healthcare). B-values (0, 50, 800, 1200 s/mm^2) were acquired with monopolar gradients along 3 orthogonal directions (TR/TE

= 3400/86 ms, pix.dim. = 1.88x1.88 mm, slice thickness = 3 mm, num. of slices = 22, acquisition time = 4.6min).
In order to estimate SNR, for each repetition an image of only noise was acquire, by turning off any excitation pulse.
The same protocol for $T_{1\rho}$ and $T_{2\rho}$ imaging used for the repeatibility study was performed on one subject with the suspect of PCa, by using an ERC coil, as required by the clinical protocol usually performed at the CMRR. Successively, the biopsy confirmed the presence of cancer (GG1) and benign prostatic hyperplasia. We performed the same protocol for $T_{1\rho}$ and $T_{2\rho}$ imaging we used for the repeatibility study.

Table 2.3: Acquisition parameters for the relaxometry protocol.

3D Gradient Echo	
Repetition Time	2400 ms
Echo Time	3,18 ms
Train of HS pulses	0, 4, 8, 12 16
HS pulse duration	6 ms
Field of View	220x220x30 mm^3
Pixel dim.	1.4x1.4 mm
Slice thickness	3 mm
Signal averages	1
Acquisition Time	5.04min

Image pre-processing $T_{1\rho}$ and $T_{2\rho}$ maps were calculated with a mono-exponential fit performed in MATLAB, according Eq. (1.23). ROIs were manually drawn in the peripheral and central zone on $T_{2\rho}$-weighted image, by referring to the T_2-weighted image. The identification of ROI was made on $T_{2\rho}$-weighted since it showed a better contrast between PZ and CG than $T_{1\rho}$-weighted image.
Mean and standard deviation were calculated in ROIs for each relaxation time.
In the subject with PCa, $T_{1\rho}$, $T_{2\rho}$, ADC and T_2-weighted values

were calculated in BPH and healthy tissue. Since the lesion was too small, it was impossible to draw a reliable ROI in PCa tissue. SNR was calculated as described in Section 2.2.2, but noise was estimated from the noise image.

Statistical analysis The intraclass correlation coefficient (ICC) was used to assess the repeatability of measurements [67], taking into account two sources of variability, between-subject and between-scans within the subject. Since there was no systematic difference between the repeated scans, we considered both between-subject and within-subject sources of variability as independent random effects, therefore ICC(1,1) model was used [92].

2.3 Results and discussions

In this section results and the relative discussions of our four experiments on prostate imaging are reported.
The first paragraph refers to the high resolution imaging on normal and cancer human prostate tissues, performed with ultra-high magnetic field (9.4T) to approach the cellular scale and quantify diffusion parameters in the different prostate microstructures (stroma, lumen, epithelial tissue).
In the second paragraph, we investigated the ability of DTI, performed with different b-value range, to discriminate both PCa vs. normal tissue and low- vs. high-grade PCa on human subjects with biopsy-proven prostate cancer.
In the third paragraph, we discussed the diagnostic accuracy of DKI in identifying and classifying PCa by using histogram analysis.
The fourth paragraph concerns the work conducted at the Center for Magnetic Resonance Research (CMRR) of Minneapolis. These preliminary experiments were dedicated to $T_{1\rho}$, $T_{2\rho}$ imaging of prostate cancer with a fast acquisition technique, recently developed at the CMRR, that allowed imaging prostate with a good resolution (1.4x1.4mm in plane) in roughly 5 minutes of

acquisition, enabling the use of $T_{1\rho}$, $T_{2\rho}$ imaging for clinical purposes.

2.3.1 Ex-vivo micro-imaging outcomes

High resolution DWI and diffusion parameters maps of normal tissue clearly showed the prostate glandular structure, except for FA and KFA maps, that showed hyper-intensity in the stroma compartment (Fig. 2.7). The parameter that seemed to better represent tissue histo-architecture was D_K. No evident glandular structure is visible either in DWI and diffusion maps of PCa tissue (Fig. 2.7).
Compared to normal tissue, in PCa we found lower MD, D_K and K values and higher FA and KFA values (Fig. 2.6).

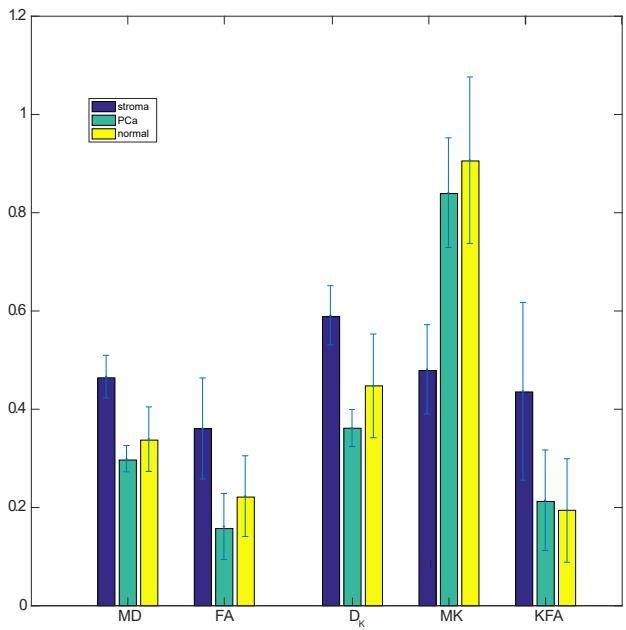

Figure 2.6: *Bargraphs show mean value and standard error of diffusion metrics calculated in stroma, PCa with GG4 and normal tissue sample, obtained from radical prostatectomy.*

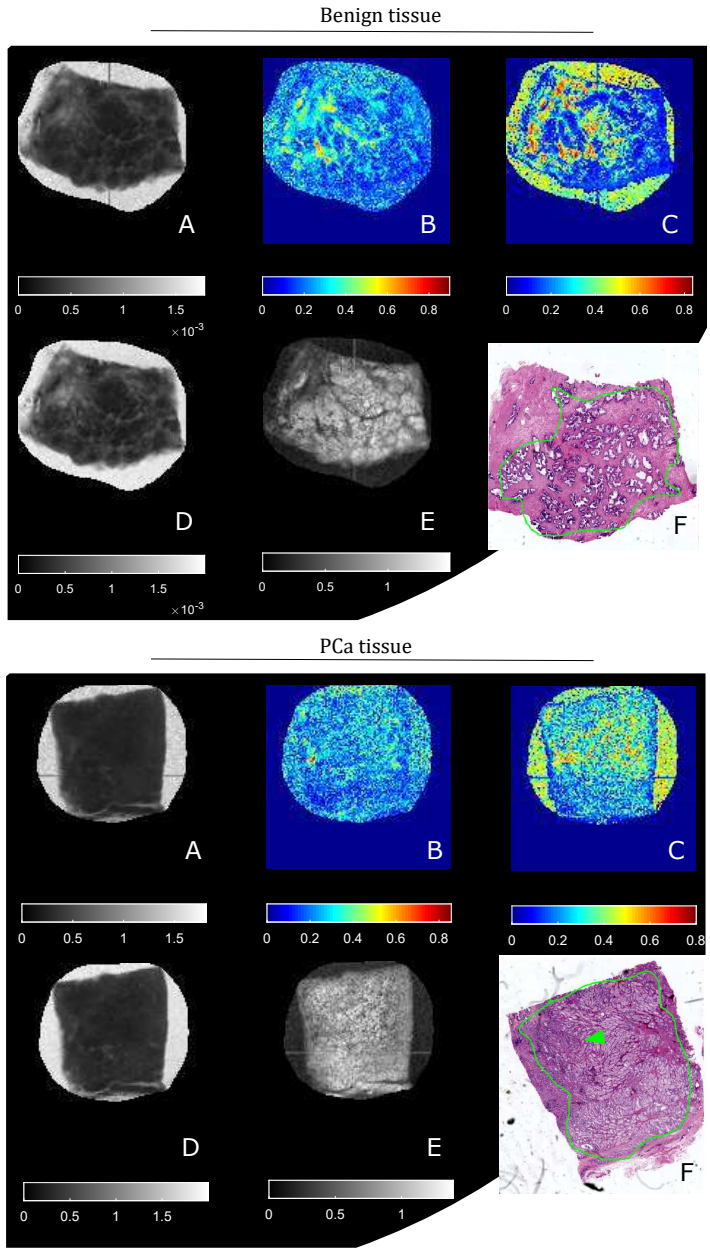

Figure 2.7: *(A-E) Respectively, high resolution MD, FA, KFA, D and K maps of a benign (top panel)and PCa (bottom panel) tissue measured at 9.4T. The pathologist highlighted in green glandular benign tissue(top) and PCa with GG4 (bottom) on the histology (F).*

Discussion This experiment was carried out to provide a direct comparison between DMRI parameters and histological assessment, that currently represents the gold standard for diagnosis. This goal is unobtainable in-vivo, where pixel dimension is 10^3 times bigger than tissue microstructures and diffusion measurements are biased by partial volume effects. With the typical resolution of in-vivo experiment (1-2mm), the DWI signal results from the overall contribution of several compartments and an incoherent orientation of stroma fibers, losing any information of micro-anisotropy.
In normal samples, DWIs and parametric maps highlighted three different diffusion compartments: ductal lumen, fibromuscolar stroma and epithelium (Fig. 2.7, top panel). Prostate glands can measure 50-100μm in diameter, therefore with a resolution of 70μm our measurements in the normal glandular structures are affected by partial volume effect; only for few bigger glands it was possible to distinguish between epithelium and lumen. Histopathological evidences showed that PCa with Gleason Score (GS) $\geq$ 4+4 consisted of a solid mass of undifferentiated cells (Fig. 2.7, bottom panel), consequently no glandular structure is recognizable on DWIs or diffusion maps of tumor samples.
MD and D_K are lower in PCa, resulting from the absence of the gland lumen and from malignant cell proliferation that obstructs the almost-free diffusion compartments (acini, ducts). However MD and D_K showed higher values in stroma than in normal tissue, probably because of the contribution of the epithelium compartment characterized by low diffusivity, as reported in another ex-vivo study [16].
Few studies [14, 16, 15, 30, 97] investigated diffusion MRI ex-vivo on prostate tissue and, to the best of our knowledge, this is the first ex-vivo study performing DKI on prostate samples, hence further investigations are necessary to clarify the role of kurtosis in ex-vivo prostate imaging.
FA and KFA showed their higher values in stroma (Fig. 2.6), whose fibrous structure exhibits micro-anisotropy, and their lower values in PCa, as a consequence of increasing cell density and

losing of the stroma compartment. In normal tissue, KFA maps seemed more rich of details compared to FA map, suggesting that would be interesting to further investigate the performance of this parameter.
Our results highlighted that diffusion derived micro-images reflect tissue architecture and structural modifications occurring with tumor. However, this experiment had one main limitation: epithelial tissue could not be segmented from lumen, since glands were too small ($\leq 50\mu m$), so it was not possible to measure diffusion parameters in these regions; this issue will be overcame by reducing pixel dimension in future experiments.
Another limitation was the scanner bore size, which allowed a maximum probe diameter of 10mm, too small to image the entire prostatectomy specimen (40-50mm diameter), preventing the co-registration of the whole histology sections to the MRI data. Moreover, it would have been interesting to evaluate the differences between TZ and PZ PCa, however, in this study, subjects were affected by PCa only in the PZ area.

2.3.2 In-vivo DTI outcomes

After the co-registration, the mutual information generally decreased, confirming the goodness of our strategy. However, the 25% of slices showed an increase of mutual information for the realignment of few b-value volumes. Mean and standard deviation (sd) of the MD and FA evaluated in PCa and normal tissue at three b-value ranges are reported in Table 2.4.
MD and FA measured in PCa developed in TZ and PZ were not statistically different, therefore, TZ and PZ lesions were considered together in the statistical analysis.
SNR was greater than 10 for all subjects at the highest b-value=2500 s/mm^2, in both PCa and benign prostate regions.
MD significantly discriminated PCa from benign tissue at every b-value range (t-test with $p< 10^{-5}$), while no significant difference was found for FA.
In Fig. 2.8, an example of MD and FA maps is displayed for four

patients with diagnosed PCa of GG1 (GS = 3 + 3), GG2 (GS = 3 + 4), GG3 (GS = 4 + 3) and GG4 (GS = 4 + 4).
MD values showed significantly linear correlation with GS (Table 2.5); the strongest correlation was observed for MD values estimated with b-value range = 0-2500 s/mm^2.

Table 2.4: MD and FA values in benign tissue and PCa measured at different b-values range.

	MD (mm^2/s)		**FA**	
	benign	PCa	benign	PCa
0-1000	1.60±0.27	0.74±0.15	0.22±0.09	0.30±0.11
0-1500	1.20±0.19	0.60±0.09	0.22±0.07	0.27±0.10
0-2500	0.80±0.11	0.46±0.07	0.21±0.06	0.26±0.08

Table 2.5: Pearson's test for the correlation between MD and GG

b-range (s/mm^2)	p-value	r
0-1000	10^{-3}	-0.38
0-1500	10^{-4}	-0.43
0-2500	10^{-4}	-0.51

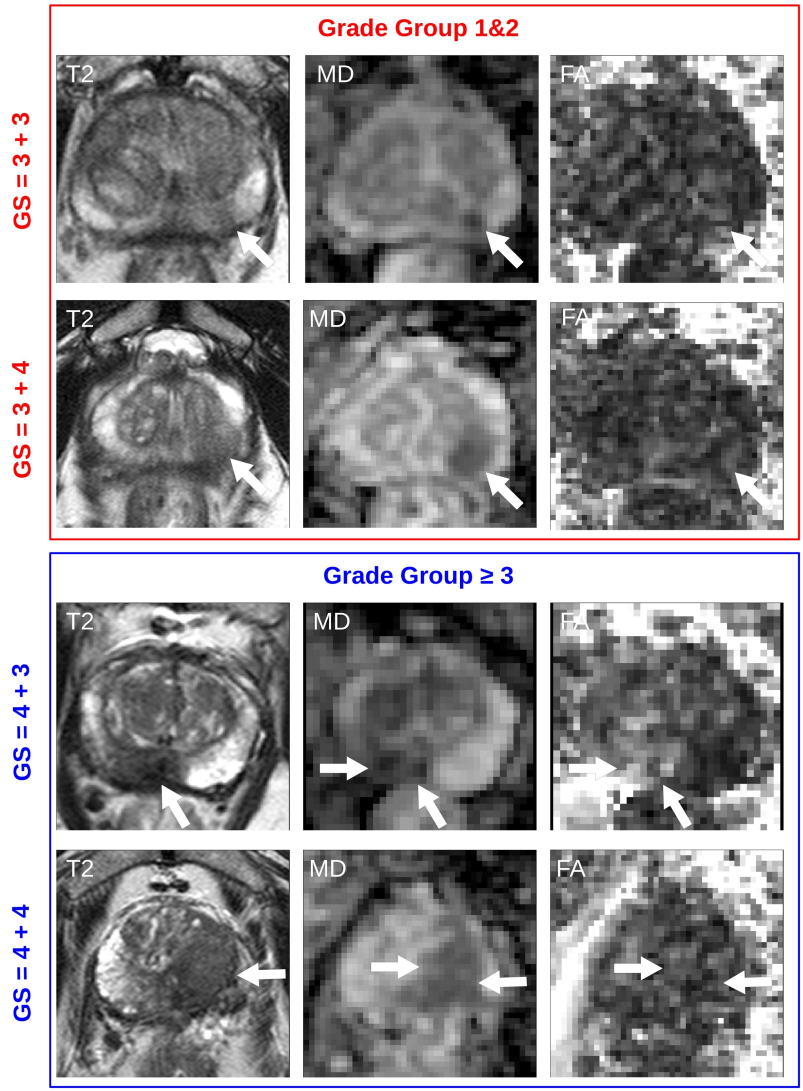

Figure 2.8: *MD and FA maps obtained in four patients with PCa of GG1 (GS=3+3), GG2 (GS=3+4), GG3 (GS=4+3) and GG4 (GS=4+4). White arrows indicate the PCa zone. T_2-weighted and DTI maps representative of low-risk and intermediate/high-risk PCa are displayed in the red and blue box, respectively. MD maps show a good contrast between cancer and benign tissue, while in FA maps lesions not recognizable.*

MD significantly discriminated between GG1-2 and GG3 in all the considered b-value ranges (Table 2.6). Moreover, the MD discriminated between GG1 and GG2 only when the b-value range = 0-1500 s/mm^2 was used. MD values were significantly different between GG1-2 and GG4, GG1-2 and GG5 and also between benign prostatic tissue and PCa of GG 1-2 (Table 2.6).
The ROC analysis showed MD calculated with b-values = 0-2500 s/mm^2 to have the highest accuracy in discriminating GG 1-2 vs. GG3 and GG1-2 vs. GG≥3 (Table 2.7).
No correlation between FA values and GS was found; therefore, the FA did not discriminate between different GGs, at any investigated b-values range, as well as FA values were not significantly different between normal and cancer tissue.

Table 2.6: ANOVA-test performed to compare MD between different GGs

b-range (s/mm^2)	0-1000	0-1500	0-2500
GG1-2 vs benign	10^{-18}	10^{-18}	10^{-20}
GG1-2 vs GG $\geq$ 3	10^{-3}	10^{-5}	10^{-5}
GG1 vs GG2	n.s	0.03	n.s.
GG1-2 vs GG3	0.03	0.01	0.01
GG1-2 vs GG4	0.04	10^{-3}	10^{-4}
GG1-2 vs GG5	$3{\cdot}10^{-4}$	10^{-4}	10^{-4}

Table 2.7: ROC curve analysis to evaluate the MD ability to discriminate GG1-2 vs GG3 and GG1-2 vs GG≥3

AUC	0-1000	0-1500	0-2500
GG1-2 vs GG3	0.78	0.74	0.82
GG1-2 vs GG≥3	0.74	0.81	0.83

Discussion In this study, we performed DTI by using three different b-values ranges: 0-1000 s/mm^2, 0-1500 s/mm^2, 0-2500

s/mm^2, highlighting how the diagnostic potential of MD values depends on the choice of b-values.
We found a significant difference in MD values between GG1-2 vs. GG3 and GG1-2 vs. GG≥3. The sensitivity of MD values in discriminating low- and high-grade PCa can be explained by considering how tumor development modifies the tissue microstructure. In particular, while GG1-2 (GS3 + 3 and GS3 + 4) is characterized by the presence of few well-formed glands, GG3 consists of poorly-formed/fused/cribriform glands and a greater amount of stroma and connective tissue, since it is mainly composed by the Gleason pattern 4 [28].
Compared to the almost free-diffusion experienced in gland lumen and ducts, water molecules motion is hindered in stroma and cribriform glands causing decreased MD values in GG3. In the same way, MD values in GG4-5 showed significantly lower values compared to GG 1-2 and GG3, due to further reduction of glands and lumen, up to their disappearance, and a predominance of fibro-muscular stroma and undifferentiated cells, causing strongly restricted and slower water diffusion.
Moreover, to discriminate between GG1-2 and GG3 with the best accuracy, this study suggests to estimate the MD by using b-value range = 0-2500 s/mm^2. The choice of b-values determines the dynamic probed by diffusion, in particular, the DWI signal acquired with high b-values is sensitive to restricted and hindered diffusion that is mainly observed in high-grade PCa. Therefore, our results indicate that diffusion MRI with high b-values should be investigated to improve the sensitivity and specificity in distinguishing between low- and intermediate/high-risk cancer in prostate tissue.
Our results showed a linear negative correlation between MD values and GS, in agreement with other studies [62, 91]. However, in contrast with Li et al. [62] and in accordance with Uribe et al. [91], we found no significant correlation between FA values and GS. Moreover, FA was not significantly different between GG1-2 and GG≥3. A possible explanation of this discrepancy could be that in Uribe et al. [91] and our study DWI was performed with

only 6 diffusion gradient directions, while Li et al. [62] used 32 directions. Since the estimation of FA strongly depends on the number of the diffusion gradient directions, the potential diagnostic role of FA should be further investigated.
The International Society of Urological Pathology [28] underlined that there is a significant difference in terms of prognosis between GG1-2 and GG≥3, since the latter has a higher recurrence rate after treatment and more frequent metastases than GG1-2, which is classified as low-risk cancer. Therefore, a reliable and non-invasive diagnostic imaging method, able to differentiate between low and intermediate/high risk PCa, is highly desirable to plan cancer treatment. Our results showed that DTI protocol can help to achieve this goal.
Finally, ROC analysis confirmed that the MD estimated with b-values = 0-2500 s/mm^2 can classify low and high-grade PCa with the highest accuracy, suggesting that high b-values should be employed in the study and diagnostic of PCa.
However, performing DTI with high b-values, albeit it was largely and successfully used in clinical imaging, it's an approximation. The diffusion tensor is calculated from a series of mono-exponential equations, yet experimentally the DWI signal deviates from the mono-exponential decay at b-values $\geq$ 1500 s/mm^2. Therefore, we continued our study on MRI clinical application on prostate cancer, by performing DKI that better describes DWI signal at high b-values.
This study was limited by a small and inhomogeneous statistical sample, since we analyzed a low number of patients with GG4-5, because thanks to the early diagnosis patients with GG1-2 or GG3 are more common. Furthermore, we correlated our DTI data with the histology results of the TRUS-MRI fusion-biopsy, not with surgical specimens of the whole prostate.

2.3.3 In-vivo DKI outcomes

In both PCa and benign prostate tissue, we measure SNR higher than 10 at the highest b-value=2500 s/mm^2, among the entire

cohort.
Statistically significant differences were found between PCa and benign tissue for DTI (MD, FA) and DKI parameters (K, D, KFA) with $p < 10^{-3}$. PT tissue was significantly different from PCa tissue (except for K, KFA_{p90} and FA) and from benign tissue for all parameters (Fig. 2.9).

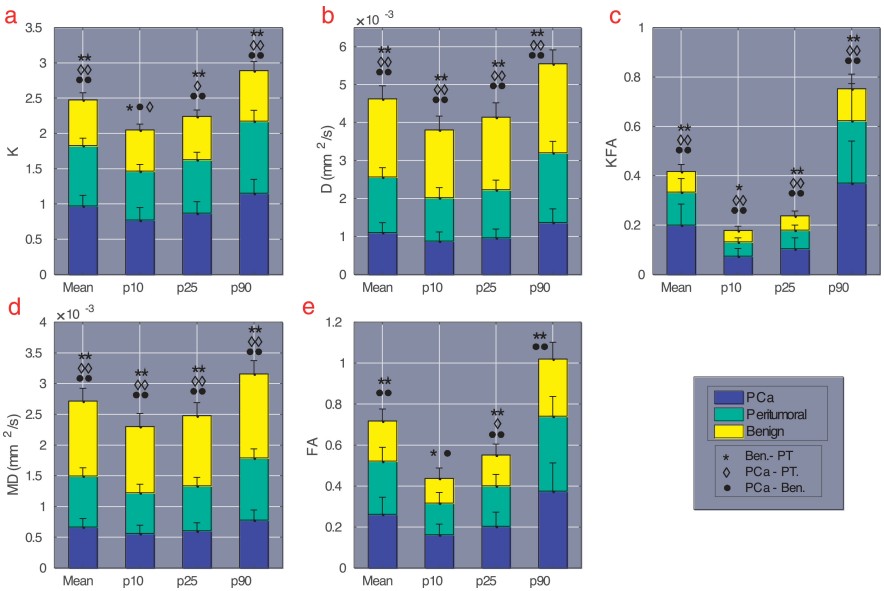

Figure 2.9: *Diffusion measures in PCa, PT, and benign regions. Stacked bargraphs show mean and SD of histogram metrics calculated in PCa (blue bars), PT (light green bars), and benign (yellow bars) tissue for each diffusion parameter: K (a), MD (b), D (c), KFA (d), and FA (e). Symbols indicate the p-value of Kruskal–Wallis test performed between PT and benign (∗), PCa and PT (◇), and PCa and benign tissue (●). ∗ $p < 0.05$; ∗∗ $p<0.001$.*

K-histogram derived parameters exhibited a strong positive correlation with tumour grade (r_m=0.51, r_{p25}=0.42, r_{p90}=0.52, $p < 0.009$, Table 2.8), except for the 10^{th} percentile. Among histogram metrics of D, only the 10^{th} percentile was weakly correlated with GG (r_{p10}=-0.36, $p < 0.03$). The mean, 10^{th} and 25^{th}

percentile of MD showed a weak negative correlation with GG (r_m=-0.36, r_{p10}=-0.41, r_{p25}=-0.39, $p < 0.05$).
No significant correlations were found between KFA and FA vs. their histogram-derived measures and vs. the tumour grade (Table 2.8).
Except for FA and KFA, diffusion maps showed a good contrast between PCa and benign tissue (Fig. 2.10). The ROC curve

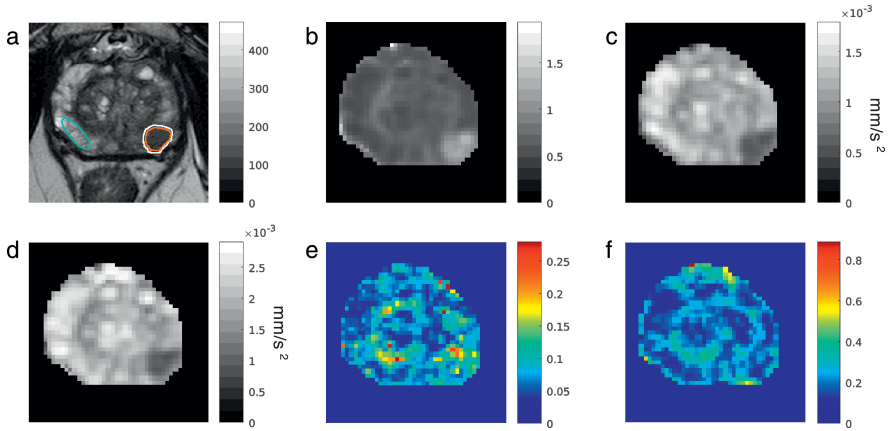

Figure 2.10: *Diffusion parametric maps. T_2-weighted image (a) with outlined PCa (orange), PT (white), and benign ROI (light blue), K-map (b), MD-map (c), D-map (d), KFA-map (e) and FA-map (f) of a subject with a GG3 lesion.*

analysis (Table 2.9) suggested that K_{p90} has the best diagnostic accuracy, i.e. the higher AUC, in distinguishing low- from high-grade PCa, (AUC=0.84), followed by MD_{p10} (AUC=0.72), D_{p10} (AUC=0.67) and KFA_{p25} (AUC=0.67), (Table 2.9). Histogram metrics of FA showed a performance similar to a random classifier with the maximum AUC=0.55 for FAm.
Histograms of diffusion metrics of one patient with GG1 and one patient with GG4, randomly chosen, are showed in Fig. 2.11.
Scatterplots in Fig. 2.12 pointed out the relationship between DKI and DTI parameters, while the results of their correlation (Pearson's test) are reported in Table 2.10.

Table 2.8: Correlation coefficient r and p-value of the Spearman's test between histogram metrics of diffusion parameters and GG ($p<0.03$)

	Mean	p10	p25	p90
K	0.51	n.s.	0.42	0.52
D	n.s.	-0.36	n.s.	n.s.
KFA	n.s.	n.s.	n.s.	n.s.
MD	-0.36	-0.41	-0.39	n.s.
FA	n.s.	n.s.	n.s.	n.s.

Table 2.9: AUC of the ROC Curve Analysis Results Obtained for Histogram Metrics of Each Diffusion Parameter

	K	D	KFA	MD	FA
Mean	0.79	0.62	0.61	0.69	0.55
p10	0.69	0.67	0.66	0.72	0.50
p25	0.74	0.64	0.67	0.71	0.50
p90	0.84	0.63	0.59	0.65	0.51

Table 2.10: Pearson's Test Results of the Correlation Between DTI and DKI Parameters evaluated in low-GG, high-GG and benign tissue ($p<0.05$).

	low-GG	high-GG	benign
K vs MD	-0.71	-0.85	-0.89
D vs MD	0.93	0.79	0.96
KFA vs FA	0.54	n.s.	0.62

Discussion In this study, we investigated the performance of DKI compared to DTI in PCa grading, using the histogram analysis.
Since low SNR can bias diffusion parameters estimation, to validate the reliability of the quantified metrics, we calculated the SNR of DWIs as a function of b-values. We found that the SNR was higher than 10 for b=2500 s/mm^2 for each patient, a value well above the critical value SNR=3 [52].
Diffusion maps (Fig. 2.10) clearly showed the presence and the extension of cancer tissue, except for FA and KFA maps. FA map showed no contrast between PCa and benign tissue, while in KFA map (e) PCa appears slightly more intense than benign tissue, not sufficiently, however, to correctly individuate PCa region or PCa extension.
Our estimation of DKI parameters in benign and cancerous prostate tissue was in general accordance with other studies, that referred a SNR 29.3±9.9 [83] and 34.81±6.44 [87] (both calculated at b=2000 s/mm^2), comparable to the mean values calculated in this study, where SNR was 18.02±7.4 (calculated at b=2500 s/mm^2) in PCa region.
Interestingly, by comparing results obtained at 3T in-vivo and at 9.4T ex-vivo, we measured higher values of MK in normal tissue than in PCa ex-vivo (Fig. 2.6), the opposite respect to what has been found in-vivo both in this and in other works [27, 83, 87, 94]. Probably, this is due to the fact that ex-vivo we measured diffusion parameters in normal tissue without segmentating lumen and epithelial tissue. Therefore, the presence of the epithelial tissue, a compartment characterized by highly restricted diffusion, exhibiting a non-Gaussian behaviour, contributed to increase MK.
In literature, the outcomes of DKI in PCa diagnosis are discordant, including studies that found an increased value for DKI in PCa assessment [27, 83, 87, 94] and studies that found no significant advantages in using DKI for PCa detection and grading [81, 90].
In our work, K showed a superior diagnostic power in discrimi-

nating low- and high-grade PCa. This is probably because, unlike previous studies that used 3 diffusion gradient directions, we have evaluated K using six gradient directions and we used a different classification of tumour grades [28, 76] with a different definition of low- and high-risk PCa.
Results of this study showed that DTI and DKI with entire-lesion histogram analysis enable the discrimination between patients with PCa of different aggressiveness grades. In agreement with Wang et al. [94], K_{p90} showed the strongest correlation with GG and the best diagnostic ability in differentiating high- from low-grade PCa, according to the ROC analysis.
MD histogram metrics showed good performance in correlating with GG and in differentiating low- and high-risk patients; however, K-metrics showed the strongest correlation with GG and the highest AUC.
By examining histograms of low- and high-grade tissues (Fig. 2.11), it is evident that K showed the largest separation. Besides, K-histogram was broader in high-grade than in low-grade tissue. This may be due to the peculiar structural heterogeneity of high-grade PCa characterized by great irregularity of glands shape and arrangement.
Conversely, the high variability of MD and D in low-grade cancer tissue (broader histograms) may reflect the presence of several diffusion compartments characterized by fast and hindered diffusion dynamics that tend to vanish when glandular structure is disrupted by high-grade cancer, resulting in distributions peaked at low diffusion values for high-grade PCa regions.

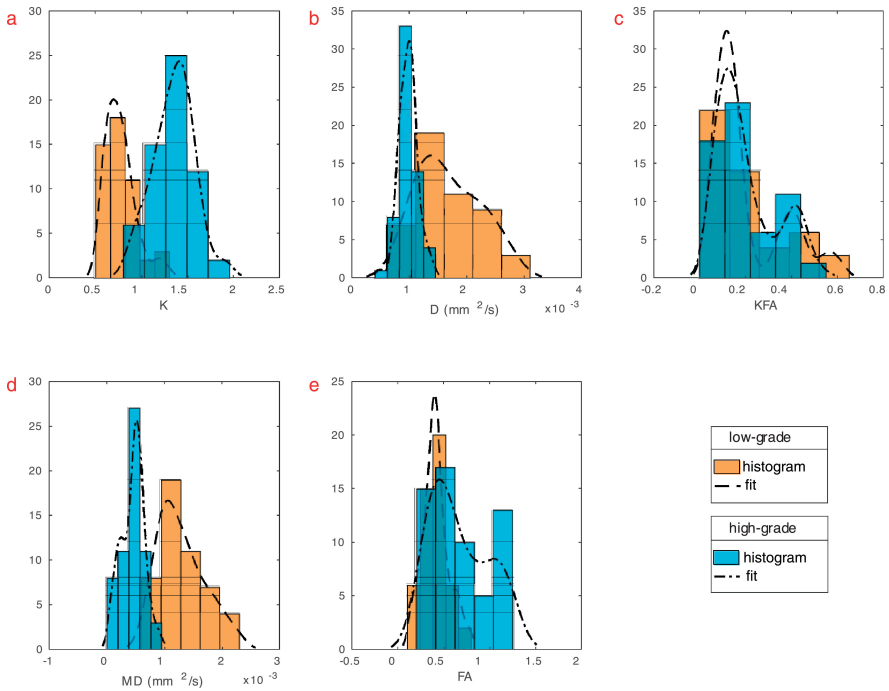

Figure 2.11: *Histograms of low- and high-GG prostate tissue. Distribution of DKI and DTI parameters of two subjects, randomly chosen, representing low- and high-GG prostate tissue (GG1 and GG4, respectively).*

Furthermore, the surrounding region of PCa lesion (peritumoral, PT) may provide cues on the prognosis and aggressiveness of the lesion itself. For example, mast cells in PT region promote angiogenesis and can be prognostic markers in prostate cancer [51]; moreover, the peritumoral lymphatic vessel density varies with the Gleason score and with the presence of regional lymph node metastases [82]. Therefore, a precise evaluation of PT region may increase the accuracy in the definition of tumour extension, and potentially provide information about future developments of the lesion. We tested the sensitivity of diffusion parameters with respect to the PT tissue, finding a statistically significant difference between the PT region and both PCa and

benign tissue, suggesting diffusion properties of this transitional zone distinct from both the benign and cancer tissues.

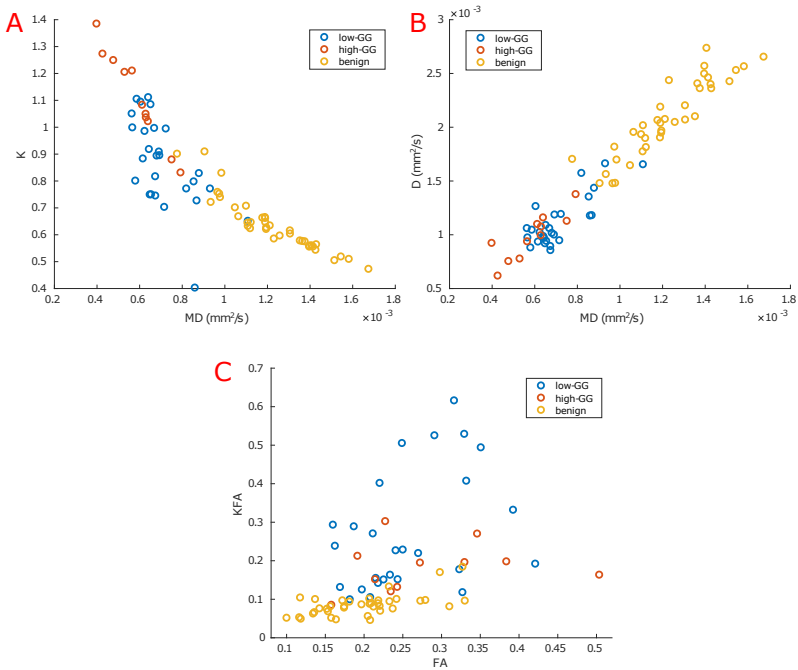

Figure 2.12: *Correlations between DTI and DKI parameters measured in benign (yellow), low-GG (blue), and high-GG (orange) prostate tissue. A: K and MD show a general inverse correlation, weaker for low-GG PCa. B: D and MD are highly correlated. C: KFA and FA are uncorrelated in high-GG PCa and moderately correlated in benign and low-GG tissue.*

As indicated by their strong correlation (Fig. 2.12B), MD and D reflected the properties of prostate tissue similarly. In fact, according to previous studies [27, 83, 87, 94], we found MD and D to be lower in cancer tissue, because of infiltrating malignant cells restricting water molecular motion. Conversely, K assumes higher values in PCa, reflecting the increased complexity and heterogeneity of tumour histo-architecture.
The variations of tissue diffusion properties are strictly related to

the morphological modifications caused by PCa: glands change in size and shape and malignant cells infiltrate ducts and acini, reducing the free available space for molecular motion [45]. The general inverse correlation between K and MD (Fig. 2.12A) pointed out how the overall effect of these micro-modifications is a combination of reduced diffusivity and increased tissue heterogeneity. However, in low-grade PCa data (GG $\leq$ 2, blue data in Figure 2.12A), the correlation between K and MD (Table 2.10) is weaker than in benign and high-GG. In particular, K values showed higher variability than MD values in low-risk PCa (Fig. 2.12A), likely that K is able to discriminate further differences in low-GG tissue, not detectable by conventional DTI analysis.
In principle, tissue anisotropy could be a marker for tumour development, since Lawrence et al. [59] showed that stroma significantly decreases in PCa. Moreover, Bourne et al. [16] underlined that stroma is a prostate compartment where micro-anisotropic diffusion occurs. Therefore, in this study, for the first time, we estimated the anisotropic complexity of benign tissue and PCa by calculating KFA values. Hansen and Jespersen [41] investigated with simulations KFA and FA in brain as a function of tissue complexity and they demonstrated that KFA can reveal tissue anisotropic complexity when FA fails, providing a different image contrast and additional information on tissue composition. However, the estimation of FA in prostate tissue generated contrasting results. As reported in Section 2.3.2, we found the FA to have no diagnostic power in classifying PCa and identify PCa from normal tissue, accordingly to the study of Xu et al. [97] where no significant FA differences between cancerous and benign tissue with both in vivo and ex vivo experiments were observed. Conversely, other authors [89] found FA to be higher in PCa and strongly correlated with GS, while Uribe et al. [91] found a weak correlation. In our study, we tested the possibility that KFA overcomes FA limitations. We found KFA to discriminate PCa from benign tissue, ROC analysis showed KFA to have a better performance than FA (AUC[KFA_{p25}]=0.67, AUC[FA_{p25}]=0.55), but neither KFA nor FA were correlated with GG. Since KFA

and FA appeared uncorrelated in high-risk PCa and moderately correlated in low-GG and in benign tissue (Fig. 2.12C, Table 2.10), KFA could furnish unexplored characteristics of prostate cancerous tissue. However, more studies should be addressed to evaluate KFA in prostate PCa at different Gleason.
One of the limits of this work was the restricted number of analysed patients, as well as the in-homogeneous distribution of specimens with different GG. Another limitation lies in the fact that TRUS-MRI fusion-biopsy was used as reference standard, because it under-estimates tumour grade in comparison to prostatectomy [58]. Finally, since we acquired DWI using six diffusion gradient directions, we could not calculate the kurtosis tensor, whose estimate needs at least 15 gradient directions [49]. Therefore, we measured the apparent kurtosis metrics, which is not rotationally invariant.
In conclusion, DKI metrics in prostate tissues provide independent and complementary information to that acquired with DTI metrics, especially in low grade PCa. As a consequence, DKI together with DTI metrics can more comprehensively characterize the complex mechanisms underlining PCa-related changes than conventional diffusion techniques alone. The DWI protocol for apparent kurtosis estimation presented here, provided an accurate tumor grades classification in a short scanning time, guaranteeing its clinical feasibility.
K-maps better highlight differences between low- and high-grade PCa and provide images with different normal/cancer tissue contrast, that could be helpful to identify smaller lesions. Furthermore, DKI yielded a better diagnostic accuracy in PCa stratification, suggesting that DKI is more sensitive to tissue microchanges occurring with tumour progression compared to DTI.
Thus, this work suggests that DKI may be useful to ameliorate the precision in the diagnosis and grading of PCa, providing different information to DTI in contained acquisition time.

2.3.4 $T_{1\rho}$ and $T_{2\rho}$ outcomes

Preliminary tests conducted on a prostate phantom in order to verify the feasibility of 3D reconstruction and the image quality are showed in Fig. 2.13. In the figure, 2D and 3D acquisition performed both with surface and ERC coil are reported.

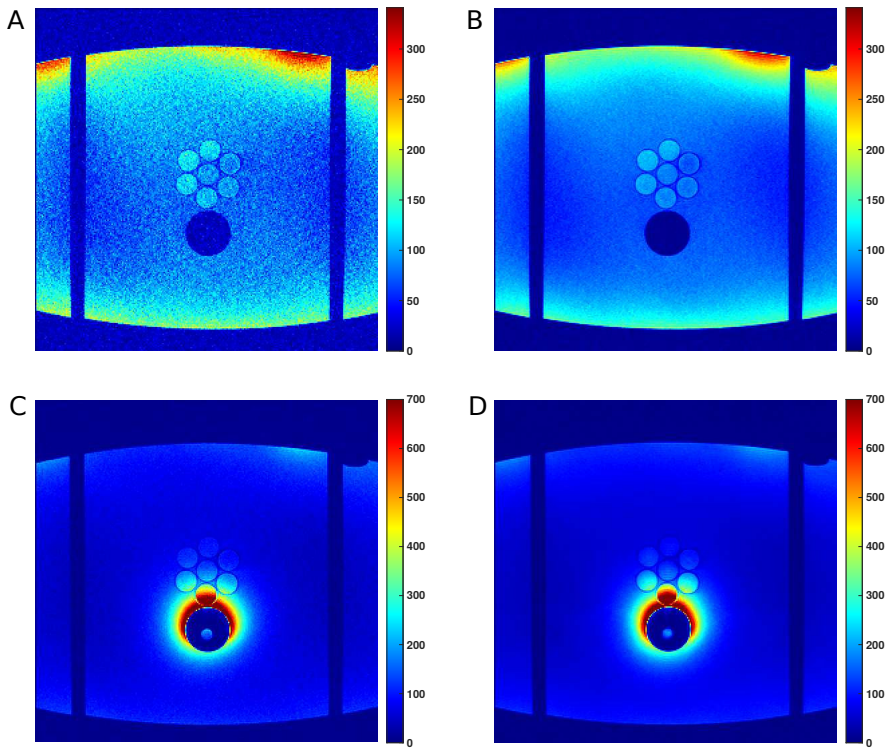

Figure 2.13: *An example of $T_{1\rho}$-weighted image acquired with 2D (A,C) and 3D (B,D) gradient echo readout by using a surface coil (A,B) and ERC coil (C,D) on a prostate phantom.*

Relaxation times measured with 2D and 3D acquisition methods were compared in 4 healthy volunteers with surface coil and 1 healthy voluneteer with ERC coil. For both $T_{1\rho}$ and $T_{2\rho}$, measurements performed with the 3D GRE and 2D GRE differed within one standard deviation for each subject (Table 2.11).

In Fig. 2.14 and 2.15 are reported respectively the SNR es-

Table 2.11: Mean and standard deviation of $T_{1\rho}$ and $T_{2\rho}$ measured with 2D and 3D reconstruction methods by using surface and ERC coil.

	$\mathbf{T_{1\rho}}$ **(s)**		$\mathbf{T_{2\rho}}$ **(s)**	
	2D	3D	2D	3D
surf. coil	0.14±0.04	0.19±0.07	0.13±0.03	0.10±0.02
ERC coil	0.30±0.07	0.21±0.03	0.08±0.03	0.08±0.02

timated in PZ and CG and a comparison between the SNR of images acquired with 2D and 3D GRE for both $T_{1\rho}$ and $T_{2\rho}$-weighted images.

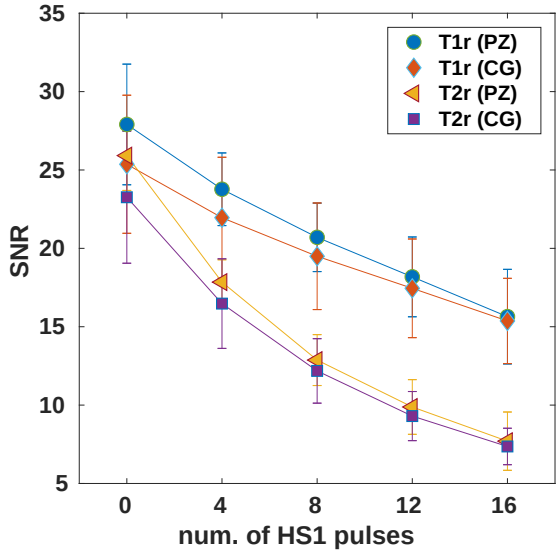

Figure 2.14: *SNR estimated in $T_{1\rho}$ and $T_{2\rho}$-weighted imaging acquired with the 3D GRE sequence. SNR was calculated in PZ and CG of healthy subjects.*

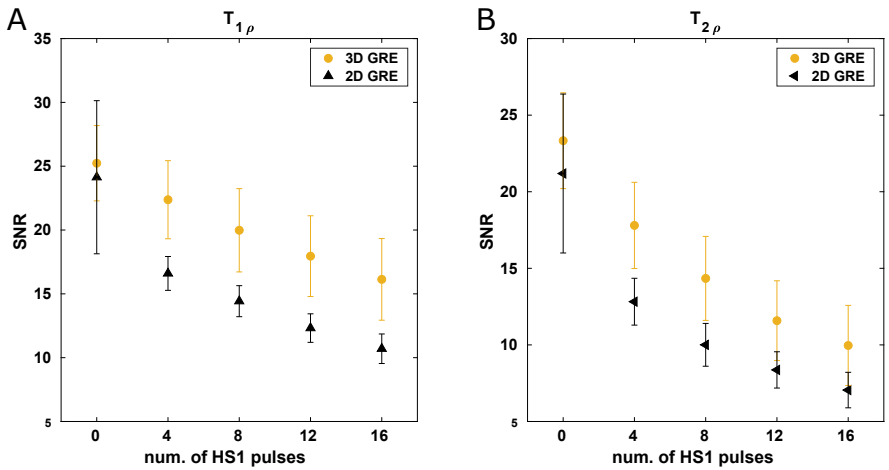

Figure 2.15: *Comparison between SNR of 2D and 3D GRE sequence for $T_{1\rho}$ (A) and $T_{2\rho}$-weighted (B) images. SNR was estimated in PZ and CG of healthy subjects.*

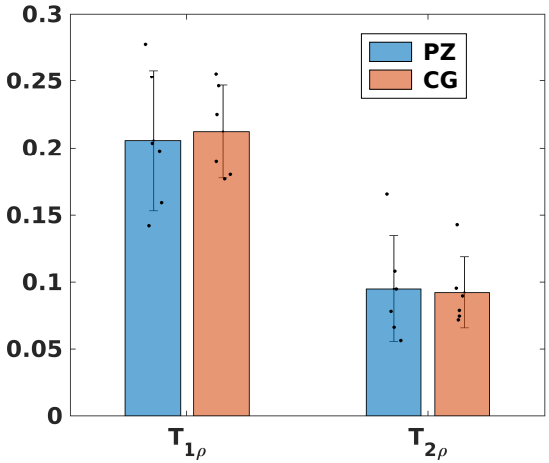

Figure 2.16: *Mean and standard deviation of $T_{1\rho}$ and $T_{2\rho}$ estimated in PZ and CG of healthy subjects.*

A comparison between prostate phantom images acquired with the 2D and 3D methods $T_{1\rho}$ and $T_{2\rho}$ values measured in PZ and CG are showed in Fig. 2.16.
In general, $T_{2\rho}$-weighted images showed a better contrast between different prostate regions than $T_{1\rho}$-weighted (Fig. 2.18), for this reason they were used for the ROI identification.
The results of the ICC test are showed in Fig. 2.17.

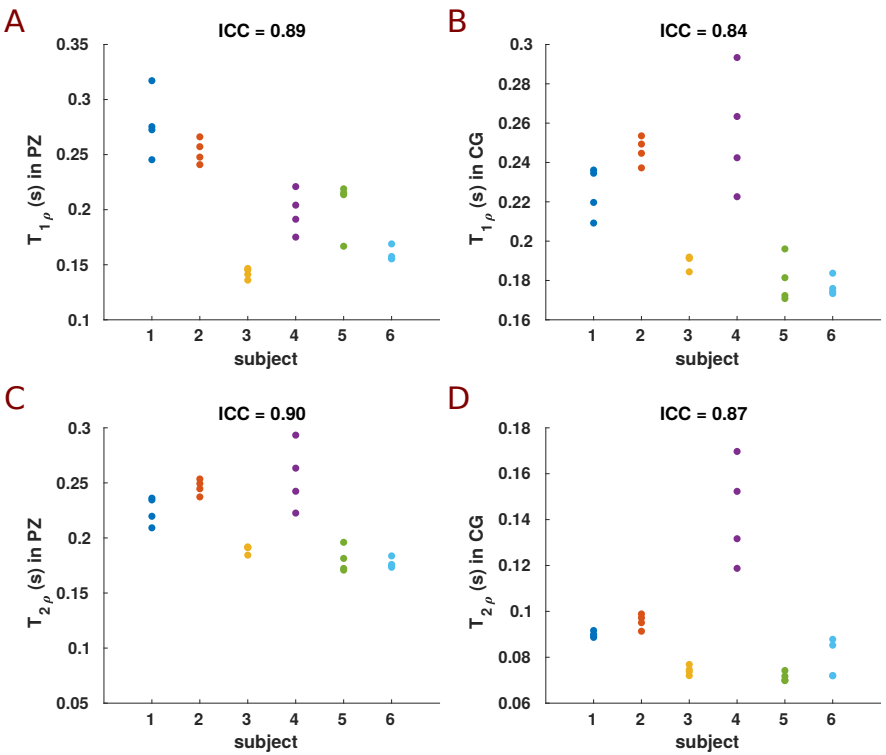

Figure 2.17: *Scatterplot of $T_{1\rho}$ (A,B) and $T_{2\rho}$ (C,D) estimated respectively in PZ and CG of healthy subjects. For each subject the measurements were repeated four times. The result of the ICC test is reported in each figure title.*

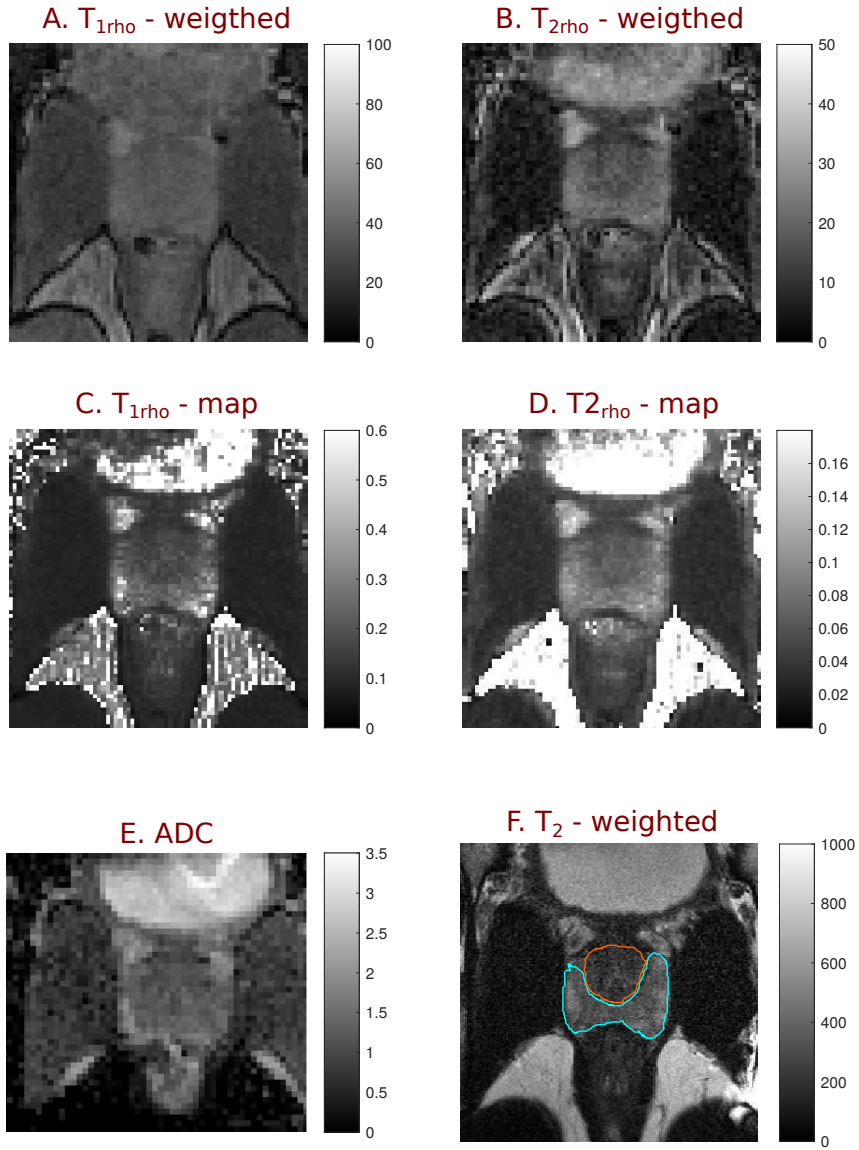

Figure 2.18: *$T_{1\rho}$ and $T_{2\rho}$-weighted images at TSL=4 (A and B); $T_{1\rho}$ and $T_{2\rho}$-map in ms (C and D) and ADC-map in mm/s^2 (E). In T_2-weighted image (F) examples of ROIs in PZ (light blue) and CG (orange) are showed.*

Preliminary results on the subject with PCa (Fig. 2.19) showed that $T_{2\rho}$ provided the best discrimination between BPH, PZ and TZ.
Also $T_{1\rho}$ histograms showed well separated mean values, while T_2-weighted and ADC values showed an overlap between BPH and PZ. (Fig. 2.20).

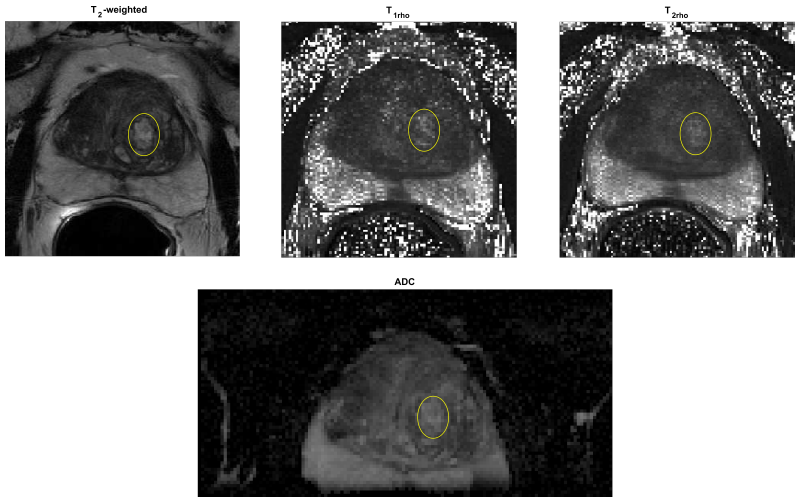

Figure 2.19: *$T_{1\rho}$, $T_{2\rho}$, ADC and T_2-weighted images acquired with ERC coil. The BPH is highlighted in yellow.*

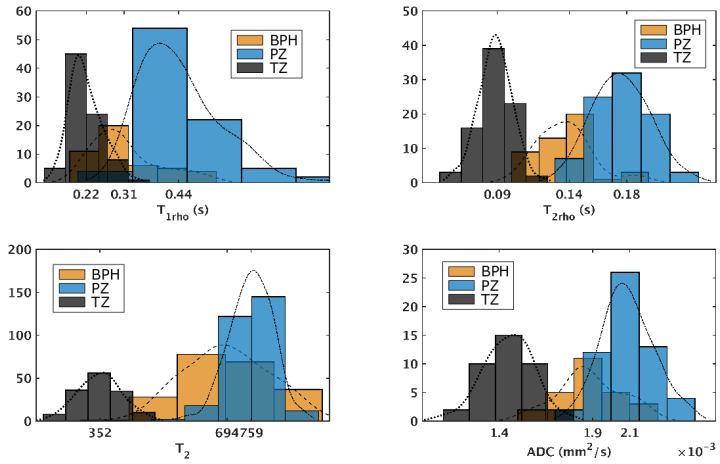

Figure 2.20: *Histogram of $T_{1\rho}$, $T_{2\rho}$, ADC and T_2-weighted values estimated in BPH and normal PZ and TZ tissue of one subject with GG1 PCa.*

Discussion In this preliminary experiment we tested the feasibility of $T_{1\rho}$ and $T_{2\rho}$ imaging in healthy prostate gland, performing a repeatability test.
A common drawback of $T_{1\rho}$ and $T_{2\rho}$ imaging is the high level of energy deposited by the sequence, estimated by specific absorption rate SAR, since the preparation pulses are applied every TR. Usually, in order to comply with the maximum allowed SAR, the TR is increased, resulting in long acquisition times.
In this study, we overcame these shortcomings by using a 3D gradient echo sequence as readout. Moreover, the 3D acquisition method provided a better SNR, as shown in Fig. 2.15, allowing to reduce the image resolution to 1.4x1.4mm, keeping the acquisition time of roughly 5min.
A preliminary study on a prostate phantom was realized to verify the image quality and the feasibility of the 3D reconstruction method. Results reported in Fig. 2.13 show a significant improvement in terms of SNR and signal homogeneity for the 3D method, remarkably visible when the surface coil was used.

In order to assess the reliability of our experimental protocol, $T_{1\rho}$ and $T_{2\rho}$ values obtained with 3D and 2D reconstruction methods were compared. $T_{1\rho}$ seemed to show an higher variability than $T_{2\rho}$, however both parameters varied within one standard deviation for each subject, both when surface and ERC coil was used (Table 2.11).
Results of the ICC test on healthy subjects suggested that our protocol provided a reliable and stable estimation of $T_{1\rho}$ and $T_{2\rho}$ (Fig. 2.17).
Preliminary results on a patient with diagnosed PCa and BPH suggested that $T_{1\rho}$ and $T_{2\rho}$ imaging could be useful to identify BPH. Given their sensitivity to tissue microenvironment [66], $T_{1\rho}$ and $T_{2\rho}$ could enable a better discrimination of benign and malignant conditions. Studies conducted on humans reported variation in the inflammatory microenvironment of BHP [5, 101]. Our measurements in BHP and normal prostate suggested that $T_{2\rho}$ had a better discrimination compared to ADC, T_2 and $T_{1\rho}$. Likely, inflammatory changes involve metabolic processes to whom relaxation in the rotating frame can be sensitive, without causing a structural change that can lead to a variation of the ADC or T_2.
These preliminary results are not sufficient to clarify the role of $T_{1\rho}$ and $T_{2\rho}$ in the diagnosis of BHP, but they suggest that further investigation should be performed.
In this work, cancer tissue could not be analyzed, since the lesions were too small to correctly identify ROIs. However, our work demonstrated the feasibility of $T_{1\rho}$ and $T_{2\rho}$ imaging in prostate cancer by using a 3D gradient echo readout, which enable to acquire 5 volumes with a good resolution (1.4x1.4mm in plane) in less than 5min, making these techniques feasible for clinical applications. To the best of our knowledge, this is the first work performing $T_{1\rho}$ and $T_{2\rho}$ with a 3D reconstruction technique and the first one performing $T_{2\rho}$ imaging on prostate. There is only another one work performing $T_{1\rho}$ imaging of prostate cancer [47], which showed the ability of $T_{1\rho}$ to differentiate low- and high-grade PCa. Our estimation of $T_{1\rho}$ on healthy tissue are in good

accordance with the measurements reported by Jambor et al. [47].
The 3D method allowed $T_{1\rho}$ and $T_{2\rho}$ imaging with a good resolution, an higher SNR in a reasonable acquisition time, while the 2D approach would have required 20min for the same image geometry.

Chapter 3

Fetal brain development

The versatility of Diffusion MRI and its sensitivity to probe tissue microstructure even with a simple and fast imaging protocol allowed us to conduct an intriguing study on fetal brain development.
The fascinating process of brain development involves a highly organized mechanism of cell proliferation, histogenesis and myelination leading to the formation of 100 billion neurons in neonatal brains [3].
This study investigated in-vivo fetal brains affected by ventriculomegaly disease, in comparison with normal cases. We were able to image fetal brain from the 19^{th} to the 38^{th} gestational week, without using any sedation both for fetuses and mothers.
VM is one of the most common diseases in fetuses, being diagnosed in approximately 1 out of every 1000 live births [78], at any gestational age (GA), with a 36,7% probability of survival without disability [21]. Moreover, VM has been associated with numerous neurological conditions, such as autism [74], epilepsy [46] and schizophrenia [96]; however, DWI studies in fetal brain during gestation are scarce.
An important prognostic factor is whether VM is associated with other abnormalities, since fetuses manifest normal neurological development in the majority of isolated mild VM cases [44]. So far, it is not understood why mild VM can cause motor and cog-

nitive disturbances to the newborn, unlike some cases of severe VMs. For this reason, it is necessary to develop new diagnostic markers to better understand this type of pathology.
The superiority of MRI in identifying fetal brain anomalies, with respect to the sonography [34, 64, 99], suggests further investigations on prenatal imaging and DWI is one of the best candidates, given its sensitivity for micro-structural changes.
Prenatal MRI is mainly performed at 1.5T to reduce heating effects and potential risks of the radio-frequency exposure [95], which limits image resolution and signal-to-noise ratio (SNR). Another limitation for fetal imaging is artifact due to motion of both the fetus and mother. In small brains, particularly in the second trimester of gestation, low resolution prevents a correct selection of brain regions and therefore the accuracy of measurements, causing ADC values to be biased by partial volume effects. Studies in fetuses are limited and usually lack an appropriate preprocessing of raw data to improve the quality and reliability of the results [39, 43, 85, 98]. In this work, we investigated the potential ability of DWI denoising methods [93] and artifact corrections [48, 54] to assess unbiased ADC values for characterizing normal and VM fetal brain development.
Towards this goal, we used a rapid DWI protocol to measure ADC in fetal brains at different gestational ages, in the second and third trimester of gestation. With the aim to establish normative ADC measurements, which will be useful to compare and identify cases with anomalies, this study analyzed variations in ADC during gestation of healthy fetuses, compared to cases of fetuses with mild, moderate and severe VM.

3.1 Materials and Methods

DWI was performed in 58 singleton fetuses during the second and third gestational trimester at 1.5T (Siemens Avanto, Erlangen, Germany), without mother-fetal sedation.
Thirty-one fetuses presenting ventricular dilatation (VD) on ultrasound investigation were referred to the Radiological Sciences

Department of Sapienza University (Rome, Italy) for MRI scans to further assess brain pathologies. Atrial diameter was measured on ultrasound and MRI according to the International Society of Ultrasound in Obstetrics and Gynecology (ISUOG) guidelines [2] and ventriculomegaly (VM) was defined when the atrial diameter of one or both ventricles was $\geq$ 10 mm. The final cohort consisted of 31 fetuses with isolated VM and 27 normal fetuses, that is, with atrial diameter $<$ 10 mm. In 12 cases, VM was diagnosed as mild (VD $<$ 12 mm), in 8 as moderate (VD between 12-14 mm) and in 10 as severe (VD $\geq$ 15 mm). None of the fetuses showed cerebral anomalies observable with conventional MRI examination, consisting of T2-weighted and FLAIR images. The study was conducted with the approval of the local Ethics Committee after obtaining a written informed consent from all the mothers.

Imaging protocol Pregnant women were examined in supine position with a phased-array coil placed over the pelvis. Before performing MRI, a multi-planar scanogram was obtained to localize the fetus.
The Diffusion MRI protocol included a DW-Spin Echo EPI with repetition time (TR) = 4000 ms, echo time (TE) = 79 ms, bandwidth = 1628 Hz/px, matrix dimension = 192x192, field of view (FOV) = 379 mm^2, in-plane resolution = 2x2 mm^2, slice-thickness = 4 mm, number of signal averages (NSA) = 2.
Preliminary tests were performed on three fetuses to carefully choose the diffusion directions and weightings for the Diffusion MRI protocol. B-values were selected to reduce perfusion effects on ADC estimation and minimize the scanning time to obviate fetal motion. These tests were performed with b-values = 0, 10, 30, 50, 100, 200, 400, 700 s/mm^2, according to a typical Intra-voxel Incoherent Motion (IVIM) protocol [61, 100]. We evaluated ADC in a region of white matter (WM) and a region of grey mater (GM) using an IVIM model, mono-exponential model with b-values = 0, 50, 200, 700 s/mm^2 and mono-exponential model with b-values = 50, 200, 700 s/mm^2. As shown in Fig. 3.1C, the

fast decay of the diffusion-weighted signal, mainly due to perfusion, is strongly reduced at b-value = 50 s/mm^2. Therefore, from the comparison between diffusion parameters estimated using IVIM and mono-exponential models, we selected b-values = 50, 200, 700 s/mm^2 for the diffusion protocol used to acquire data from all subjects of the healthy and VM cohorts. The total scan time was approximately 2 minutes.

Pre-processing and data analysis After a first inspection, 2 normal and 11 VM cases (2 mild, 2 moderate, 7 severe) showed motion artifacts impossible to correct or severe ventricle dilatation that prevented correct ROI selection; thus 13 subjects were discarded from the following analysis.
The pipeline for image correction (Fig. 3.1) started with noise removal by using *dwidenoise* tool [93]; then, *unring* [54] was used to correct *denoised* DWI for Gibbs-ringing artifacts. Eventually, images were corrected for fetal/mother motion artifacts by using FLIRT [48]: each volume was registered to the image at b-value = 50 s/mm^2 through a rigid-body transformation, using a trilinear interpolation method.
Seven regions of interest (ROI) were manually placed in the centrum semiovale (CSO), frontal white matter (FWM), occipital white matter (OWM), thalamus (TH), basal ganglia (BG), cerebellar hemispheres (CH) and pons, as reported in Fig. 3.1B. In some VM cases, ROIs could not be placed in CSO (3 cases), FWM (3), BG (3), TH (3), OWM (3), CH (1) because VM was severe or the brain was too small.

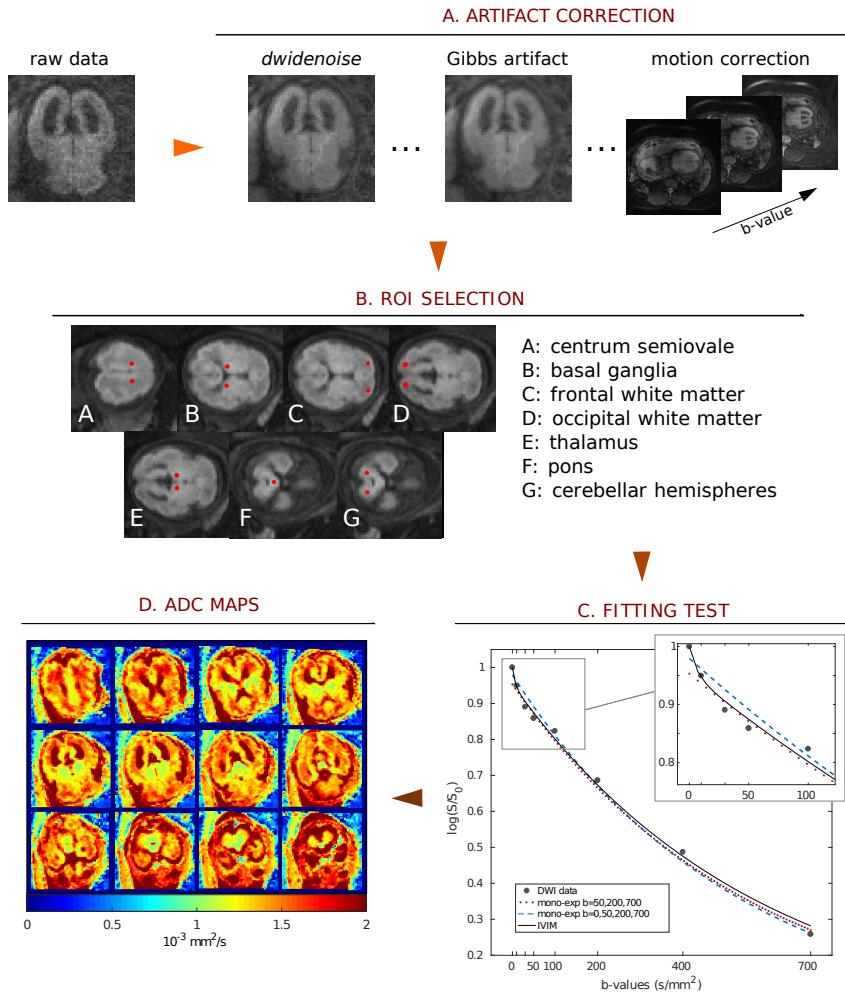

Figure 3.1: *Scheme of image analysis. A: Raw images were first corrected for noise, Gibbs and motion artifacts. B: Seven ROIs were manually drawn. C: In preliminary tests on 3 subjects we compared 3 fitting procedures to evaluate perfusion effects of DWI signal: 2 mono-exponential fit (with b-values = 50, 200, 700 s/mm^2 and b-values = 0, 50, 200, 700 s/mm^2) and an IVIM fit (with b-values = 0, 10, 30, 50, 100, 200, 400, 700 s/mm^2). The magnification highlights the greater slope of the mono-exponential fit with b = 0 caused by perfusion. D: Finally, ADC maps were calculated by mono-exponential fit with b-values = 50, 200, 700 s/mm^2.*

SNR of raw and corrected DWI at each b-value was calculated to evaluate the reliability of estimated ADC values. SNR was calculated in each volume as the ratio between DWI signal averaged over all brain ROIs and the standard deviation (SD) of noise, as follows:

$$SNR = 0.655 \frac{mean(signal)}{SD(noise)} \tag{3.1}$$

where noise was estimated in the background and the factor 0.655 was used to account for Rayleigh distribution of background noise [26].
ADC values were measured through a fitting procedure developed in MATLAB, with a linear least-squares algorithm, and the goodness-of-fit was evaluated with the root mean squared error (RMSE). The fitting procedure was carried out voxel-by-voxel, making inter-volume motion correction a mandatory step for voxel alignment.

Statistical analysis ADC values were measured through a fitting procedure developed in MATLAB, with a linear least-squares algorithm, and the goodness-of-fit was evaluated with the root mean squared error (RMSE). The fitting procedure was carried out voxel-by-voxel, making inter-volume motion correction a mandatory step for voxel alignment.
A multi-way ANOVA with Bonferroni correction was used to evaluate differences in ADC between normal and VM cases and between the second and third TR.
The relationship between ADC measurements and GA was assessed with linear and quadratic regression analysis by calculating the adjusted coefficient of determination R^2 and the p-value for the Fisher-test to evaluate the statistical significance of the model. Initially, linear regression was performed in each ROI. However, we observed that some brain regions (FWM, OWM and BG) showed an evident non-linear dependence on GA, thus we performed a quadratic regression in those regions. Outliers,

that is values bigger than three median absolute deviations away from median, were not considered in the regression analysis.

3.2 Results and discussions

The preliminary tests, performed to choose the optimal b-values of the Diffusion MRI protocol for reducing perfusion effects on ADC measurements, showed a fast decay of the DWI signal due to perfusion at low b-values ($b \leq 50$ s/mm^2). However, the fast signal decay was strongly reduced at b-values=50 s/mm^2 (Fig. 3.1C). Therefore we performed the study using b-values equal to 50, 200, 700 s/mm^2. Moreover, the ADC estimated by the mono-exponential function with three b-values did not differ more than the SD the from the diffusion coefficient derived by the only diffusion component of the IVIM model, estimated with eight b-values.
SNR and the quality of DW-images considerably increased after noise and artifact correction ($\text{SNR}_{corr} = 19.5 \pm 7.8$, $\text{SNR}_{raw} = 7.8 \pm 3.1$; both calculated at b-value = 700 s/mm^2), as shown in Fig. 3.2A. Also the goodness-of-fit significantly increased after correction ($\text{RMSE}_{\text{raw}} = 0.07$, $\text{RMSE}_{\text{corr}} = 0.06$, p = 0.0001, Fig. 3.2B).

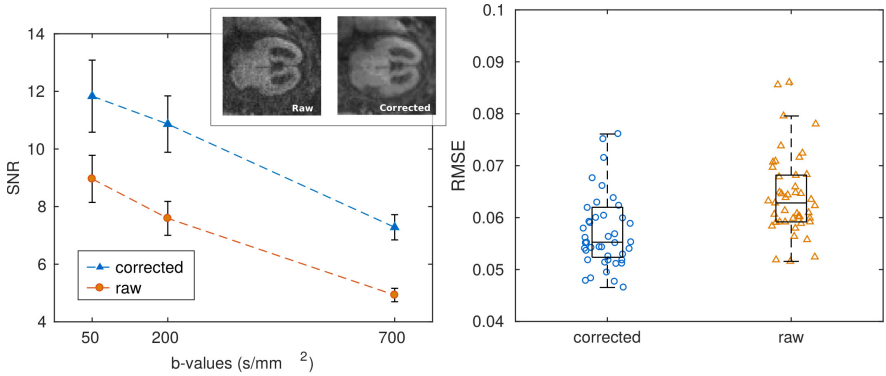

Figure 3.2: *A: Mean and standard error of SNR calculated over the entire patient cohort. An example of raw and corrected DWI at b-value = 700 s/mm^2 is reported in the top right corner of the plot. B: Boxplots of the root mean squared error of ADC fit; dots represent RMSE for each subject averaged over the ROI.*

Mean ADC values in normal and VM fetuses, obtained in the second and third trimester of gestation and in different cerebral regions, are shown in Fig. 3.3. Significant differences were found between second and third trimester in CSO, FWM, TH, CH and pons of both normal and VM brains ($p \leq 0.03$). ADC values in normal and VM ROIs were not significantly different, except for CSO and FWM ($p \leq 0.02$).

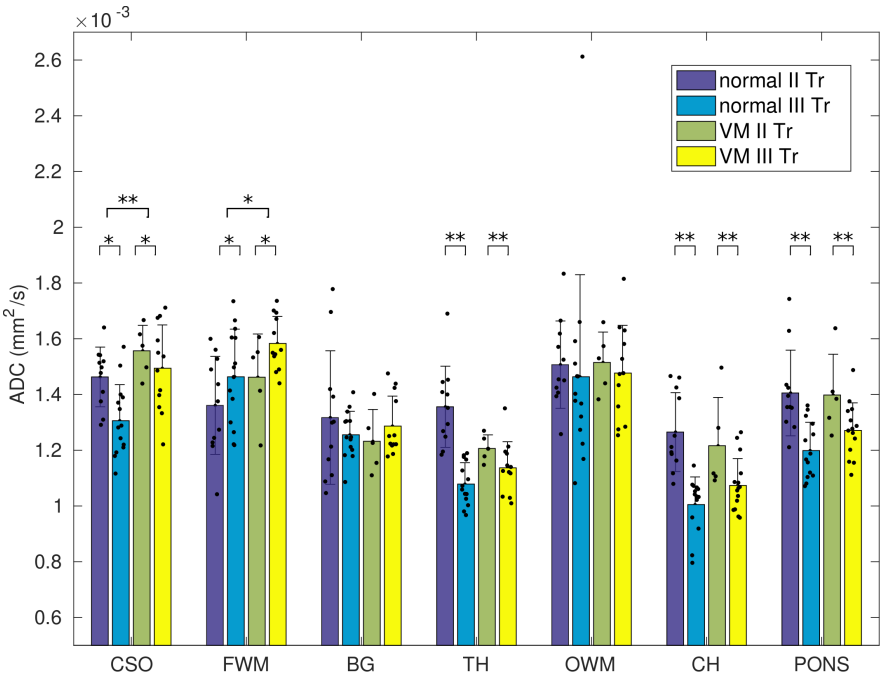

Figure 3.3: *ADC measurements in normal and VM brains of fetuses in the second and third trimester of gestation. Dots represent the ADC calculated for each subject and asterisks represent the p-value of multi-way ANOVA (* $p < 0.02$; ** $p < 10^{-3}$).*

Linear regression analysis showed ADC values in CSO, TH, CH and pons to significantly decrease with GA both in normal ($p \leq 0.001$; Fig. 3.4 (A, B, D, E) and Table 3.1) and VM brains ($p \leq 0.001$; Fig. 3.4 (G, H, J, K) and Table 3.1). A significant quadratic relationship with GA was found in BG and OWM of normal brains ($p \leq 0.02$; Fig. 3.4 (C, F) and Table 3.1) and FWM of VM cases ($p \leq 0.02$; Fig. 3.4I and Table 3.1).
In the entire data set, 6 outliers were found in TH ($1.68 \cdot 10^{-3}$mm^2/s), BG ($1.77, 1.69 \cdot 10^{-3}$mm^2/s), OWM ($2.68 \cdot 10^{-3}$mm^2/s) and CH ($1.74 \cdot 10^{-3}$mm^2/s) for normal brains and in pons ($1.49 \cdot 10^{-3}$mm^2/s) for VM brains; these values were discarded from both linear and quadratic regression analysis.

Table 3.1: Regression analysis between ADC and Gestational Age

	Normal				**VM**			
	Linear		**Quadratic**		**Linear**		**Quadratic**	
	R^2	p	R^2	p	R^2	p	R^2	p
CSO	.36	.001	-	-	.28	.02	-	-
FWM	-	ns	-	ns	-	ns	.34	.02
BG	-	ns	.19	.04	-	ns	-	-
TH	.82	$< 10^{-5}$	-	-	.36	.006	-	-
OWM	.17	.02	.54	.0001	-	ns	-	ns
PONS	.54	$< 10^{-3}$	-	-	.48	$< 10^{-2}$	-	-
CH	.65	$< 10^{-4}$	-	-	.38	.003	-	-

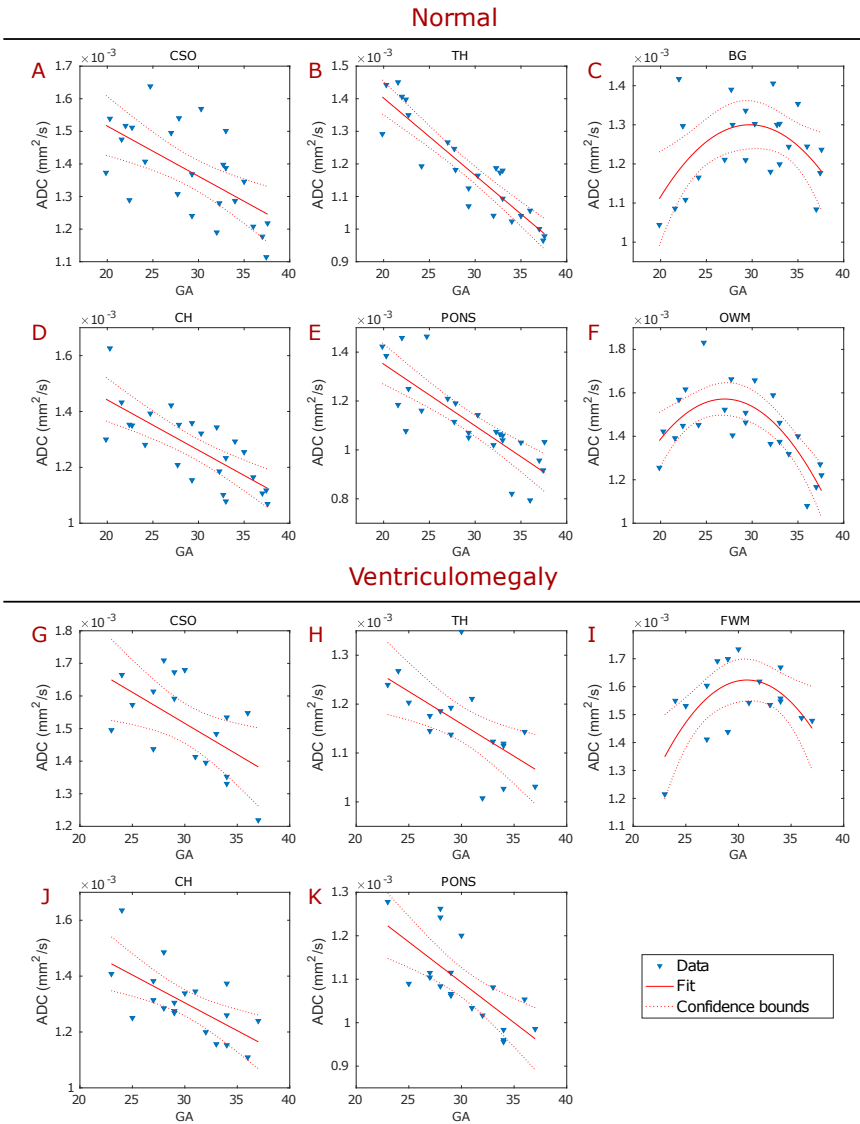

Figure 3.4: *Regression analysis of the ADC in normal (upper panel) and VM (lower panel) fetal brains showed the changes of biological water diffusion as a function of the gestational age (GA). Each plot, showing data fit and 95% confidence interval, refers to a particular ROI: CSO, TH, BG, CH, pons and OWM of normal brains (A-F) and CSO, TH, FWM, CH and pons of VM cases (G-K), respectively.*

Discussion In this work, prenatal DWI was performed at 1.5T and the ADC was measured in fetal brains during the second and third trimester of gestation, both in normal and VM cases.
Prenatal imaging could be strongly affected by uncontrollable fetal/mother movement, especially when performed without sedation. In order to limit motion-derived artifacts, we designed our DWI protocol with limited number of signal averages (NSA = 2) to be as fast as possible, causing poor SNR (SNR_{raw} = 7.8 ± 3.1 at b = 700 s/mm^2) in our data. To overcome image quality limitations, raw data were denoised and corrected for motion and Gibbs' ringing artifacts. Results, reported in Fig. 3.2A, showed that image pre-processing significantly improved SNR and goodness-of-fit, guaranteeing a better ROI selection of different fetal brain regions and a reliable estimation of the ADC. Moreover, volume registration was fundamental to minimize voxel misalignment, since the fitting procedure was carried-out voxel-by-voxel.
Since ADC estimation is strongly influenced by the diffusion weighting, in this study b-values were carefully chosen in order to minimize perfusion contamination of ADC measurements; therefore, DWI with b-value = 50 s/mm^2 was acquired as first volume and used to normalize data prior to fit. It is well known that DWI with low diffusion weighting is sensitive to perfusion motion, resulting from blood micro-circulation in capillaries [61], which contributes to increased ADC values. By normalizing diffusion data with the volume at b-value = 50 s/mm^2, we reduced the contribution of perfusion in our measurements, finding, in normal fetuses, lower ADC values compared to other studies that used b = 0 [39, 43, 85, 98].
In a recent study [100], an IVIM technique was carried out to separately measure the contribution of perfusion and diffusion, in developing fetal brain. The authors [100] measured lower ADC values in CSO, FWM, OWM, CH and pons compared to those reported in literature [39, 43, 85, 98], demonstrating that perfusion motion can affect ADC measurements in fetal brains. Our ADC values were in good accordance with the measurements de-

rived from the contribution of solely diffusion in the IVIM study [100], suggesting that our acquisition strategy effectively minimized perfusion effects.
However, authors [100] acquired DWI with nine b-values (from 0 to 1000 s/mm^2) in order to fit the IVIM model, using a total acquisition time of about 5 min. As a result of a longer acquisition time, compared to that used in this work (2 min), the IVIM study [100] discarded 56% of subjects due to fetal movements, while in this study only 22% of subjects was rejected for motion artifacts.
Analogously to other works in normal fetuses [17, 39, 43, 85, 100], we found that during brain development, ADC linearly decreased in CSO, TH, CH and pons, as well as in VM cases, reflecting the morphological changes of brain maturation that involves increasing cellularity, histogenesis and myelination [57]. The latter starts in the spinal cord (12 GA), followed by pons, cerebellar peduncles and thalamic axons (14-20 GA), in the frontal, parietal and occipital lobes (30 GA) and finally in the cortex (35 GA), lasting for decades in the human brain [7, 11, 42, 69]. The process of myelination begins with the accumulation of lipids and proteins [32] and the proliferation of oligodendrocyte precursors [6], causing a reduction of extracellular space, with a consequent decrease in ADC values. According to previous results [17, 39, 43, 85, 100], the ADC was found to be significantly higher in the fetal white matter than in the deep brain nuclei (BG, TH, and pons), suggesting an immature status of fiber myelination during fetal development.
Consistently with the timeline of myelination, we found the decrease of diffusivity in OWM (normal cases) and FWM (VM cases) to start from 28-30 GA, later than CSO, TH, CH and pons. An initial increase in ADC values was measured in cortical WM, from 23 to 30 GA, followed by a decline after 30 GA, as reported in other studies [23, 37, 84]. These results are in agreement with the normal progression of myelination that occurs from central to peripheral brain.
Although in VM fetuses no other alteration was reported by ul-

trasound exam, we found significantly higher diffusivity (Fig 3.3) in CSO and FMW compared to normal fetal brain. This result may reveal delayed or abnormal maturation of white matter, as reported in other studies in neonates with isolated mild VM [33, 35, 29], suggesting that the ADC in CSO and FWM could be a marker of altered development and disorders associated with VM.

Furthermore, regression analysis in TH showed that ADC values were more strongly correlated with GA in normal than in VM cases (Tab. 3.1 and Fig. 3.4B), while no significant correlation was found in OWM of VM cases, suggesting the possibility of a delayed white matter maturation in VM brains, especially during the third trimester of gestation.

In contrast to a recent work [98], we did not find significantly higher ADC values in BG of VM compared to normal fetuses. Anatomically, BG is the nearest structure to the lateral ventricles, hence it is more prone to be affected by signal contamination from ventricles due to volume misalignment. This could have caused the disagreement with the work of Yaniv et al. [98], since they did not use any method to realign DWI.

Moreover, the same authors [98] found lower ADC in FWM of VM fetuses compared to normal fetal brain, whereas we obtained the opposite result (Fig. 3.3). FWM and OWM regions are supplied by the carotid system with large vessels, so perfusion is relatively high, as shown in reference [100]. We suspect that ADC measured by Yaniv et al. [98] was partially affected by perfusion, since they acquired data using b-values = 0 and 700 s/mm^2, leading to the discrepancies with our results.

To the best of our knowledge, no other works have investigated the ADC in brain development of VM fetuses (Fig. 3.4(G-K)). Although our study was limited by a small statistical sample, it could help to establish criteria for recognizing abnormal brain development that is important for early diagnosis of diseases.

In addition to the small number of subjects, our study was also limited by the slice thickness, which should be reduced to minimize partial volume effects and to enable more accurate identifi-

cation of brain tissues.
Our study on VM brains revealed the sensitivity of DWI in brain diseases, making this technique suitable also to patient follow-up. Moreover, our routine image correction had proven to be a reasonable and fast method for improving the quality of diffusion-weighted images and for providing a reliable identification of ROIs.
Perfusion motion might affect DWI signal, causing ADC to be artificially higher; in this work we showed that, using b-value = 50 s/mm^2 as first acquired diffusion-weighted volume, the ADC was quantified without significant perfusion contamination, since our measurements were comparable to those obtained by the IVIM model [100].
Although our work is limited by the use of 1.5T magnetic field, our rapid acquisition protocol combined with artifact correction allowed a reliable estimation of the ADC in a very short time and the identification of anomalies in fetal brain development.
This work suggested that regional differences in fetal ADC values and their variations with GA reflect micro-structural and physiological changes due to brain maturation. These preliminary data can contribute to delineate a reference standard to assess the normal progress of sulcation and myelination as well as the normative biometry of the fetal brain, contributing to improve knowledge of brain maturation.

Conclusions

This PhD project was aimed at the optimization of MRI protocols for pelvis imaging, in particular for the diagnosis of prostate cancer (PCa) and for the study of fetal brain development.
This work investigated the potentiality of different MRI techniques to diagnose and grade PCa by using diffusion MRI and relaxation in the rotating frame imaging.
The study performed with DMRI demonstrated that the sensitivity of the diffusion parameters is enhanced when high diffusion weightings are used. Indeed, the performances of DKI, describing the diffusion signal when high b-values are involved, definitely overcame DTI diagnostic accuracy.
We demonstrated that the limit of low SNR, which affects DWI signal at high b-values, can be easily addressed by using post-processing tools to reduce noise and correct for Gibbs artifacts, providing a more accurate estimation of DKI metrics. DKI could be easily implemented in a clinical protocol, helping the identification of PCa thanks to added image contrast and tissue details.
The clinical study of DMRI was corroborated by an ex-vivo investigation where high-resolution imaging was performed. This work represented the unique occasion to directly compare diffusion measurements with histology results, which currently determine the gold standard for the diagnosis of PCa. This comparison constitutes the only way to validate measured parameters and understand what is their relationship with tissue microstructure.
Moreover, our work on rotating frame relaxation imaging demonstrated the feasibility and reliability of adiabatic $T_{1\rho}$ and $T_{2\rho}$

performed with a recently developed three dimensional acquisition approach. Given the sensitivity of $T_{1\rho}$ and $T_{2\rho}$ for tissue microenviroment, our preliminary results suggested that these parameters could be employed in the discrimination of BHP and normal tissue, a result never accomplished by any MRI parameter so far.
The three-dimensional sequence, developed at the CMRR, provided a fast reconstruction protocol for $T_{1\rho}$ and $T_{2\rho}$ imaging, making it feasible for clinical application. Indeed, the sequence we developed will be installed at the Minneapolis Health Fairview Clinics and Surgery Center for further investigation on subjects with PCa.
Furthermore, the project on fetal brain imaging suggested that a fast acquisition protocol combined with a simple post-processing pipeline enable a reliable investigation of brain development.
The protocol for fetal brain was efficiently designed to reduce the effect of perfusion on ADC measurements and simultaneously reducing the acquisition time and motion artifacts, sparing the discard of data. The necessity to provide a short and efficient image protocol limited the quality of acquired data in terms of SNR. This issue was successfully addressed with a fast post-processing pipeline, guaranteeing the reliability of estimating ADC.
In conclusion, the sensitivity of DMRI for microstructural changes in body tissue caused by cancer, brain disease or normal condition like brain maturation can be fruitfully utilized in combination with artifact correction methods. Moreover, new strategy of image reconstruction, such as 3D gradient echo, can be successfully employed to perform abdominal imaging, enriching the investigation of in-vivo systems with information on tissue microenvironment.

Bibliography

[1] P.A. Abragam and A. Abragam. *The Principles of Nuclear Magnetism*. Comparative Pathobiology - Studies in the Postmodern Theory of Education. Clarendon Press, 1961. ISBN: 9780198520146.

[2] JS Abramowicz et al. "International Society of Ultrasound in Obstetrics and Gynecology (ISUOG)". In: *Ultrasound in Obstetrics and Gynecology: The Official Journal of the International Society of Ultrasound in Obstetrics and Gynecology* 16.6 (2000), pp. 594–596.

[3] Sandra Ackerman et al. *Discovering the brain*. National Academies Press, 1992.

[4] Hashim U Ahmed et al. "Transatlantic Consensus Group on active surveillance and focal therapy for prostate cancer". In: *BJU international* 109.11 (2012), pp. 1636–1647.

[5] Paloma Alonso-Magdalena et al. "A role for epithelial-mesenchymal transition in the etiology of benign prostatic hyperplasia". In: *Proceedings of the National Academy of Sciences* 106.8 (2009), pp. 2859–2863.

[6] Stephen A Back et al. "Arrested oligodendrocyte lineage progression during human cerebral white matter development: dissociation between the timing of progenitor differentiation and myelinogenesis". In: *Journal of Neuropathology & Experimental Neurology* 61.2 (2002), pp. 197–211.

[7] AJ Barkovich et al. “Normal maturation of the neonatal and infant brain: MR imaging at 1.5 T.” In: *Radiology* 166.1 (1988), pp. 173–180.

[8] Peter J Basser and Derek K Jones. “Diffusion-tensor MRI: theory, experimental design and data analysis–a technical review”. In: *NMR in Biomedicine: An International Journal Devoted to the Development and Application of Magnetic Resonance In Vivo* 15.7-8 (2002), pp. 456–467.

[9] Peter J Basser, James Mattiello, and Denis LeBihan. “MR diffusion tensor spectroscopy and imaging”. In: *Biophysical journal* 66.1 (1994), pp. 259–267.

[10] Christian Beaulieu. “The basis of anisotropic water diffusion in the nervous system–a technical review”. In: *NMR in Biomedicine: An International Journal Devoted to the Development and Application of Magnetic Resonance In Vivo* 15.7-8 (2002), pp. 435–455.

[11] CR Bird et al. “MR assessment of myelination in infants and children: usefulness of marker sites.” In: *American Journal of Neuroradiology* 10.4 (1989), pp. 731–740.

[12] JS Blicharski. “Dipolar relaxation of several spin systems in solids”. In: *Canadian Journal of Physics* 55.1 (1977), pp. 31–37.

[13] P.A. Bottomley and J.R. Griffiths. *Handbook of Magnetic Resonance Spectroscopy In Vivo: MRS Theory, Practice and Applications*. eMagRes Books. Wiley, 2016.

[14] Roger Bourne et al. “16 T diffusion microimaging of fixed prostate tissue: preliminary findings”. In: *Magnetic resonance in medicine* 66.1 (2011), pp. 244–247.

[15] Roger M Bourne et al. “Apparatus for histological validation of in vivo and ex vivo magnetic resonance imaging of the human prostate”. In: *Frontiers in oncology* 7 (2017), p. 47.

[16] Roger M Bourne et al. “Microscopic diffusivity compartmentation in formalin-fixed prostate tissue”. In: *Magnetic resonance in medicine* 68.2 (2012), pp. 614–620.

[17] Margaretha J Brouwer et al. “Sequential cranial ultrasound and cerebellar diffusion weighted imaging contribute to the early prognosis of neurodevelopmental outcome in preterm infants”. In: *PloS one* 9.10 (2014), e109556.

[18] R.B. Buxton. *Introduction to Functional Magnetic Resonance Imaging: Principles and Techniques*. Introduction to Functional Magnetic Resonance Imaging: Principles and Techniques. Cambridge University Press, 2009. URL: https://books.google.com/books?id=U7X6nDAtA-MC.

[19] Paul T. Callaghan. *Principles of Nuclear Magnetic Resonance Microscopy*. Oxford science publications. Clarendon Press, 1993. ISBN: 9780198539971.

[20] P.T. Callaghan. *Translational Dynamics and Magnetic Resonance: Principles of Pulsed Gradient Spin Echo NMR*. OUP Oxford, 2011. ISBN: 9780191621048.

[21] Silvia Carta et al. “Outcome of fetuses with prenatal diagnosis of isolated severe bilateral ventriculomegaly: systematic review and meta-analysis”. In: *Ultrasound in Obstetrics & Gynecology* 52.2 (2018), pp. 165–173.

[22] Theresa Y Chan et al. “Prognostic significance of Gleason score 3+ 4 versus Gleason score 4+ 3 tumor at radical prostatectomy”. In: *Urology* 56.5 (2000), pp. 823–827.

[23] Vann Chau et al. “Abnormal brain maturation in preterm neonates associated with adverse developmental outcomes”. In: *Neurology* 81.24 (2013), pp. 2082–2089.

[24] Pradip Datta. “PSA in Prostate Cancer Diagnosis”. In: *The Oncogenomics Handbook*. Springer, 2005, pp. 393–402.

[25] Robin A De Graaf and Klaas Nicolay. “Adiabatic rf pulses: Applications to in vivo NMR”. In: *Concepts in Magnetic Resonance: An Educational Journal* 9.4 (1997), pp. 247–268.

[26] Olaf Dietrich et al. “Measurement of signal-to-noise ratios in MR images: influence of multichannel coils, parallel imaging, and reconstruction filters”. In: *Journal of Magnetic Resonance Imaging: An Official Journal of the International Society for Magnetic Resonance in Medicine* 26.2 (2007), pp. 375–385.

[27] Olivio F Donati et al. “Prostate cancer aggressiveness: assessment with whole-lesion histogram analysis of the apparent diffusion coefficient”. In: *Radiology* 271.1 (2013), pp. 143–152.

[28] Jonathan I Epstein et al. “The 2014 International Society of Urological Pathology (ISUP) consensus conference on Gleason grading of prostatic carcinoma”. In: *The American journal of surgical pathology* 40.2 (2016), pp. 244–252.

[29] G Lockwood Estrin et al. “Altered white matter and cortical structure in neonates with antenatally diagnosed isolated ventriculomegaly”. In: *NeuroImage: Clinical* 11 (2016), pp. 139–148.

[30] Xiaobing Fan et al. “High-resolution MRI of excised human prostate specimens acquired with 9.4 T in detection and identification of cancers: Validation of a technique”. In: *Journal of Magnetic Resonance Imaging* 34.4 (2011), pp. 956–961.

[31] Stephen J Freedland et al. “Upgrading and downgrading of prostate needle biopsy specimens: risk factors and clinical implications”. In: *Urology* 69.3 (2007), pp. 495–499.

[32] FH Gilles, W Shankle, and EC Dooling. “Myelinated tracts: growth patterns”. In: *The developing human brain*. Elsevier, 1983, pp. 117–183.

[33] John H Gilmore et al. “Prenatal mild ventriculomegaly predicts abnormal development of the neonatal brain”. In: *Biological psychiatry* 64.12 (2008), pp. 1069–1076.

[34] Nadine J Girard. “Magnetic resonance imaging of fetal developmental anomalies”. In: *Topics in Magnetic Resonance Imaging* 22.1 (2011), pp. 11–23.

[35] Casey B Goodlett et al. “Group analysis of DTI fiber tract statistics with application to neurodevelopment”. In: *Neuroimage* 45.1 (2009), S133–S142.

[36] Denis S Grebenkov. “Use, misuse, and abuse of apparent diffusion coefficients”. In: *Concepts in Magnetic Resonance Part A: An Educational Journal* 36.1 (2010), pp. 24–35.

[37] Patric Hagmann et al. “White matter maturation reshapes structural connectivity in the late developing human brain”. In: *Proceedings of the National Academy of Sciences* 107.44 (2010), pp. 19067–19072.

[38] Erwin L Hahn. “Spin echoes”. In: *Physical review* 80.4 (1950), p. 580.

[39] Rui Han et al. “Assessment of apparent diffusion coefficient of normal fetal brain development from gestational age week 24 up to term age: a preliminary study”. In: *Fetal diagnosis and therapy* 37.2 (2015), pp. 102–107.

[40] Benjamin F Hankey et al. “Cancer surveillance series: interpreting trends in prostate cancer—part I: evidence of the effects of screening in recent prostate cancer incidence, mortality, and survival rates”. In: *Journal of the National Cancer Institute* 91.12 (1999), pp. 1017–1024.

[41] Brian Francis Hansen and Sune Nørhøj Jespersen. “Kurtosis fractional anisotropy, its contrast and estimation by proxy”. In: (2016).

[42] Katsumi Hayakawa et al. “Normal brain maturation in MRI”. In: *European Journal of Radiology* 12.3 (1991), pp. 208–215.

[43] Chen Hoffmann et al. “Regional apparent diffusion coefficient values in 3rd trimester fetal brain”. In: *Neuroradiology* 56.7 (2014), pp. 561–567.

[44] Thierry AGM Huisman. “Fetal magnetic resonance imaging of the brain: is ventriculomegaly the tip of the syndromal iceberg?” In: *Seminars in Ultrasound, CT and MRI*. Vol. 32. 6. Elsevier. 2011, pp. 491–509.

[45] Peter A Humphrey. “Gleason grading and prognostic factors in carcinoma of the prostate”. In: *Modern pathology* 17.3 (2004), p. 292.

[46] Daren C Jackson et al. “Ventricular enlargement in new-onset pediatric epilepsies”. In: *Epilepsia* 52.12 (2011), pp. 2225–2232.

[47] Ivan Jambor et al. “Rotating frame relaxation imaging of prostate cancer: Repeatability, cancer detection, and Gleason score prediction”. In: *Magnetic resonance in medicine* 75.1 (2016), pp. 337–344.

[48] M Jenkinson et al. “FSL”. In: *NeuroImage* 62 (2012), pp. 782–790.

[49] Jens H. Jensen et al. “Diffusional kurtosis imaging: The quantification of non-Gaussian water diffusion by means of magnetic resonance imaging”. English (US). In: *Magnetic Resonance in Medicine* 53.6 (June 2005), pp. 1432–1440. ISSN: 0740-3194. DOI: 10.1002/mrm.20508.

[50] Hempel Johann-Martin et al. “Histogram analysis of diffusion kurtosis imaging estimates for in vivo assessment of 2016 WHO glioma grades: A cross-sectional observational study”. In: *European Journal of Radiology* 95 (2017), pp. 202 –211. ISSN: 0720-048X. DOI: https://doi.org/10.1016/j.ejrad.2017.08.008.

[51] Anna Johansson et al. “Mast cells are novel independent prognostic markers in prostate cancer and represent a target for therapy”. In: *The American journal of pathology* 177.2 (2010), pp. 1031–1041.

[52] Derek K Jones and Peter J Basser. ""Squashing peanuts and smashing pumpkins": how noise distorts diffusion-weighted MR data". In: *Magnetic Resonance in Medicine: An Official Journal of the International Society for Magnetic Resonance in Medicine* 52.5 (2004), pp. 979–993.

[53] David E Kang et al. "Risk stratification of men with Gleason score 7 to 10 tumors by primary and secondary Gleason score: results from the SEARCH database". In: *Urology* 70.2 (2007), pp. 277–282.

[54] Elias Kellner et al. "Gibbs-ringing artifact removal based on local subvoxel-shifts". In: *Magnetic resonance in medicine* 76.5 (2016), pp. 1574–1581.

[55] Valerij G Kiselev. "Fundamentals of diffusion MRI physics". In: *NMR in biomedicine* 30.3 (2017). DOI: 10.1002/nbm.3602.

[56] Valerij G. Kiselev. "The Cumulant Expansion: An Overarching Mathematical Framework For Understanding Diffusion NMR". In: *Diffusion MRITheory, Methods, and Applications*. Oxford, UK: Oxford University Press, Sept. 2012. ISBN: 9780195369779.

[57] Orthello Richardson Langworthy. "Development of behavior patterns and myelinization of the nervous system in the human fetus and infant". In: *Contrib Embryol* 139 (1933), pp. 3–57.

[58] Camille Lanz et al. "Gleason score determination with transrectal ultrasound-magnetic resonance imaging fusion guided prostate biopsies—are we gaining in accuracy?" In: *The Journal of urology* 195.1 (2016), pp. 88–93.

[59] Edward M Lawrence et al. "Evaluating prostate cancer using fractional tissue composition of radical prostatectomy specimens and pre-operative diffusional kurtosis magnetic resonance imaging". In: *PloS one* 11.7 (2016), e0159652.

[60] Denis Le Bihan et al. “Diffusion tensor imaging: concepts and applications”. In: *Journal of Magnetic Resonance Imaging: An Official Journal of the International Society for Magnetic Resonance in Medicine* 13.4 (2001), pp. 534–546.

[61] Denis Le Bihan et al. “Separation of diffusion and perfusion in intravoxel incoherent motion MR imaging.” In: *Radiology* 168.2 (1988), pp. 497–505.

[62] Linjun Li et al. “Effect of time scale on accounting for renewable emergy in ecosystems located in humid and arid climates”. In: *Ecological Modelling* 287 (2014), pp. 1 –8. ISSN: 0304-3800.

[63] Stacy Loeb et al. “Systematic review of complications of prostate biopsy”. In: *European urology* 64.6 (2013), pp. 876–892.

[64] Lucia Manganaro et al. “Role of foetal MRI in the evaluation of ischaemic-haemorrhagic lesions of the foetal brain”. In: (2012).

[65] Silvia Mangia et al. “Rotating frame relaxation during adiabatic pulses vs. conventional spin lock: simulations and experimental results at 4 T”. In: *Magnetic resonance imaging* 27.8 (2009), pp. 1074–1087.

[66] Antti T Markkola et al. “Determination of T1ρ values for head and neck tissues at 0.1 T: a comparison to T1 and T2 relaxation times”. In: *Magnetic resonance imaging* 16.4 (1998), pp. 377–383.

[67] Kenneth O McGraw and Seok P Wong. “Forming inferences about some intraclass correlation coefficients.” In: *Psychological methods* 1.1 (1996), p. 30.

[68] Shalom Michaeli, Dennis J Sorce, and Michael Garwood. “T2ρ and T1ρ adiabatic relaxations and contrasts”. In: *Current Analytical Chemistry* 4.1 (2008), pp. 8–25.

[69] Jeffrey H Miller et al. “Diffusion-tensor MR imaging of normal brain maturation: a guide to structural development and myelination”. In: *American Journal of Roentgenology* 180.3 (2003), pp. 851–859.

[70] James L Mohler et al. “Prostate cancer, version 1.2014”. In: *Journal of the National Comprehensive Cancer Network* 11.12 (2013), pp. 1471–1479.

[71] Pratik Mukherjee et al. “Diffusion tensor MR imaging and fiber tractography: theoretic underpinnings”. In: *American journal of neuroradiology* 29.4 (2008), pp. 632–641.

[72] Gillian Murphy et al. “The expanding role of MRI in prostate cancer”. In: *American Journal of Roentgenology* 201.6 (2013), pp. 1229–1238.

[73] Dmitry S Novikov et al. “Quantifying brain microstructure with diffusion MRI: Theory and parameter estimation”. In: *NMR in Biomedicine* 32.4 (2019), e3998.

[74] Saskia JMC Palmen et al. “Increased gray-matter volume in medication-naive high-functioning children with autism spectrum disorder”. In: *Psychological medicine* 35.4 (2005), pp. 561–570.

[75] Marco Palombo et al. “New insight into the contrast in diffusional kurtosis images: Does it depend on magnetic susceptibility?” In: *Magnetic resonance in medicine* 73.5 (2015), pp. 2015–2024.

[76] Phillip M Pierorazio et al. “Prognostic Gleason grade grouping: data based on the modified Gleason scoring system”. In: *BJU international* 111.5 (2013), pp. 753–760.

[77] Carlo Pierpaoli et al. “Diffusion tensor MR imaging of the human brain.” In: *Radiology* 201.3 (1996), pp. 637–648.

[78] Gianluigi Pilu et al. “Ultrasound of the fetal central nervous system”. In: *Current Opinion in Obstetrics and Gynecology* 12.2 (2000), pp. 93–103.

[79] Joseph C Presti Jr. “Prostate biopsy: current status and limitations”. In: *Reviews in urology* 9.3 (2007), p. 93.

[80] William S Price. *NMR studies of translational motion: principles and applications*. Cambridge University Press, 2009.

[81] Matthias C Roethke et al. “Evaluation of diffusion kurtosis imaging versus standard diffusion imaging for detection and grading of peripheral zone prostate cancer”. In: *Investigative radiology* 50.8 (2015), pp. 483–489.

[82] Andres A Roma et al. “Peritumoral lymphatic invasion is associated with regional lymph node metastases in prostate adenocarcinoma”. In: *Modern pathology* 19.3 (2006), p. 392.

[83] Andrew B Rosenkrantz et al. “Prostate cancer: feasibility and preliminary experience of a diffusional kurtosis model for detection and assessment of aggressiveness of peripheral zone cancer”. In: *Radiology* 264.1 (2012), pp. 126–135.

[84] JF Schneider et al. “Diffusion-weighted imaging in normal fetal brain maturation”. In: *European radiology* 17.9 (2007), pp. 2422–2429.

[85] Michel Manuel Schneider et al. “Normative apparent diffusion coefficient values in the developing fetal brain”. In: *American Journal of Neuroradiology* 30.9 (2009), pp. 1799–1803.

[86] Edward O Stejskal and John E Tanner. “Spin diffusion measurements: spin echoes in the presence of a time-dependent field gradient”. In: *The journal of chemical physics* 42.1 (1965), pp. 288–292.

[87] Shiteng Suo et al. “Non-Gaussian water diffusion kurtosis imaging of prostate cancer”. In: *Magnetic resonance imaging* 32.5 (2014), pp. 421–427.

[88] Alberto Tannús and Michael Garwood. "Adiabatic pulses". In: *NMR in Biomedicine: An International Journal Devoted to the Development and Application of Magnetic Resonance In Vivo* 10.8 (1997), pp. 423–434.

[89] Weizhong Tian et al. "Correlation of diffusion tensor imaging parameters and Gleason scores of prostate cancer". In: *Experimental and therapeutic medicine* 15.1 (2018), pp. 351–356.

[90] Jussi Toivonen et al. "Mathematical models for diffusion-weighted imaging of prostate cancer using b values up to 2000 s/mm2: Correlation with Gleason score and repeatability of region of interest analysis". In: *Magnetic resonance in medicine* 74.4 (2015), pp. 1116–1124.

[91] Carlos F Uribe et al. "In vivo 3 T and ex vivo 7 T diffusion tensor imaging of prostate cancer: Correlation with histology". In: *Magnetic resonance imaging* 33.5 (2015), pp. 577–583.

[92] Sharmila Vaz et al. "The case for using the repeatability coefficient when calculating test–retest reliability". In: *PloS one* 8.9 (2013), e73990.

[93] Jelle Veraart et al. "Denoising of diffusion MRI using random matrix theory". In: *NeuroImage* 142 (2016), pp. 394–406.

[94] Qing Wang et al. "Histogram analysis of diffusion kurtosis magnetic resonance imaging in differentiation of pathologic Gleason grade of prostate cancer". In: *Urologic oncology: seminars and original investigations*. Vol. 33. 8. Elsevier. 2015, 337–e15.

[95] Christian Weisstanner et al. "Fetal MRI at 3T—ready for routine use?" In: *The British journal of radiology* 90.1069 (2017), p. 20160362.

[96] Ian C Wright et al. "Genetic contributions to regional variability in human brain structure: methods and preliminary results". In: *Neuroimage* 17.1 (2002), pp. 256–271.

[97] Junqian Xu et al. “Magnetic resonance diffusion characteristics of histologically defined prostate cancer in humans”. In: *Magnetic Resonance in Medicine: An Official Journal of the International Society for Magnetic Resonance in Medicine* 61.4 (2009), pp. 842–850.

[98] Gal Yaniv et al. “Region-specific changes in brain diffusivity in fetal isolated mild ventriculomegaly”. In: *European radiology* 26.3 (2016), pp. 840–848.

[99] Shaowei Yin et al. “Contribution of MRI to detect further anomalies in fetal ventriculomegaly”. In: *Fetal diagnosis and therapy* 27.1 (2010), pp. 20–24.

[100] Xiao Yuan et al. “Fetal brain development at 25–39 weeks gestational age: A preliminary study using intravoxel incoherent motion diffusion-weighted imaging”. In: *Journal of Magnetic Resonance Imaging* (2019).

[101] Boyu Zhang et al. “Non-cell-autonomous regulation of prostate epithelial homeostasis by androgen receptor”. In: *Molecular cell* 63.6 (2016), pp. 976–989.

List of publications

Papers

- Di Trani MG, Manganaro L, Antonelli A, Guerreri M, De Feo R, Catalano C, Capuani S. Apparent Diffusion Coefficient Assessment of Brain Development in Normal Fetuses and Ventriculomegaly, *Frontiers in Physics* (2019), vol.7, pp.160.

- Di Trani MG, Nezzo M, Caporale A, De Feo R, Miano R, Mauriello A, Bove P, Manenti G, Capuani S. Performance of Diffusion Kurtosis Imaging Versus Diffusion Tensor Imaging in Discriminating Between Benign Tissue, Low and High Gleason Grade Prostate Cancer. *Academic radiology* (2019), vol.26, pp.1328-1337.

- Nezzo M, Di Trani MG, Caporale A, Miano R, Mauriello A, Bove P, Capuani S, Manenti G. Mean diffusivity discriminates between prostate cancer with grade group 1&2 and grade groups equal to or greater than 3. *European Journal of Radiology* (2016), vol.85, p.1794-1801.

Posters and talks in conference meetings

- Di Trani MG, Manganaro L, Antonelli A, Guerreri M, De Feo R, Borelli M, Pratesi G, Catalano C, Capuani S. Reliable assessment of apparent diffusion coefficient in normal and ventriculomegaly fetal brain. In: *Proceedings of the ISMRM 27th Annual Meeting & Exhibition* in Montreal, Canada, 11-16 May (2019).

- Di Trani MG, Caporale A, Nezzo M, Capuani S. Towards a definition of the biophysical bases of transient Anomalous Diffusion (TAD) parameters. Evaluation of tAD, DKI and DTI in normal and cancer prostate tissue with Magnetic Resonance micro-imaging at 9.4 Tesla. In: *Proceedings of*

the ISMRM 26th Annual Meeting & Exhibition in Paris, France, 16-21 June (2018).

- Di Trani MG, Manganaro L, Antonelli A, Guerreri M, De Feo R, Bernardo S, Catalano C, Capuani S. Apparent diffusion coefficient values of the normal foetal brain developing. In: Federico Giove. Editorial: *Proceedings of the International School on Magnetic Resonance and Brain Function - XII Workshop. Frontiers in Physics.* 23-27 May (2018).

- Di Trani MG, Caporale A, Nezzo M, Miano R, Mauriello A, Bove P, Capuani S, Manenti G. Histogram analysis of low- and high-risk prostate cancer: a comparison between Gaussian and non-Gaussian diffusion. In: *Magnetic Resonance Materials in Physics, Biology and Medicine* (2017) vol.30.

- Di Trani MG, Monti S, Cavaliere C, Aiello M, Capuani S. About the dependence of Gaussian diffusion and Kurtosis parameters on SNR in prostate DWIs. In: *Magnetic Resonance Materials in Physics, Biology and Medicine* (2017), vol.30.

- Di Trani MG, Caporale A, Nezzo M, Miano R, Mauriello A, Bove P, Manenti G, Capuani S. Non-Gaussian diffusion NMR discriminates between low- and high-risk prostate cancer. In: *Proceedings of the third Edition of Biophysics@Rome* (2017).

- Di Trani MG, Caporale A, Nezzo M, Miano R, Mauriello A, Bove P, Manenti G, Capuani S. Mean Kurtosis discriminates between low- and high-risk prostate cancer better than Mean Diffusivity does. In: *Proceedings of the ISMRM 25th Annual Meeting & Exhibition* in Honolulu, Hawaii, 22-27 April (2017).

Acknowlegments

I would like to express my deepest thanks to my advisor Dr. Silvia Capuani not only because she patiently guided my studies, but mostly because she has always inspired me and supported my every decisions, always thinking to the best for me.
With sincere gratitude I would like to thank Dr. Silvia Mangia for her precious advices and all the care she put in the work we did together. It was an enourmous pleasure working with her and Dr. Shalom Michaeli along with their group in Minneapolis.
I'm very grateful to Dr. Marco Nezzo for having always been available to discuss about every doubt on the clinical aspects of this work.
I would like to thank also Dr. Greg Metzger, whose help and advices have been fundamental for the data acquisition.
I would like to express my gratitude to Dr. Federico Giove to have always helped me with valuable suggestions and great patience.
Moreover, I would like to thank my colleagues from the Italian and American laboratory and my colleagues from the Physics department, because, first of all, they have always been my friends.
For the constant moral support and motivation, especially in the hardest moments, I will never end to thank my parents, my grandmother and my sister, that helped me every day with their infinite love.